PD CISPR TR 16-3:2020

BSI Standards Publication

Specification for radio disturbance and immunity measuring apparatus and methods

Part 3: CISPR technical reports

Documents
Document Sharing Hub

Full document details: PD CISPR TR 16-3:2020

National foreword

This Published Document is the UK implementation of CISPR TR 16-3:2020.

The UK participation in its preparation was entrusted to Technical Committee GEL/210/11, EMC - Standards Committee.

A list of organizations represented on this committee can be obtained on request to its committee manager.

This publication does not purport to include all the necessary provisions of a contract. Users are responsible for its correct application.

© The British Standards Institution 2020
Published by BSI Standards Limited 2020

ISBN 978 0 539 03852 1

ICS 33.100.20; 33.100.10

Compliance with a British Standard cannot confer immunity from legal obligations.

This Published Document was published under the authority of the Standards Policy and Strategy Committee on 30 November 2020.

Amendments/corrigenda issued since publication

Date	Text affected

Documents
Document Sharing Hub

Full document details: PD CISPR TR 16-3:2020

CISPR TR 16-3

Edition 4.0 2020-10

TECHNICAL REPORT

colour inside

INTERNATIONAL SPECIAL COMMITTEE ON RADIO INTERFERENCE

Specification for radio disturbance and immunity measuring apparatus and methods –
Part 3: CISPR technical reports

INTERNATIONAL
ELECTROTECHNICAL
COMMISSION

ICS 33.100.10; 33.100.20

ISBN 978-2-8322-8957-0

Warning! Make sure that you obtained this publication from an authorized distributor.

® Registered trademark of the International Electrotechnical Commission

Documents
Document Sharing Hub

Full document details: PD CISPR TR 16-3:2020

CONTENTS

FOREWORD 16
1 Scope 18
2 Normative references 18
3 Terms, definitions and abbreviated terms 19
3.1 Terms and definitions 19
3.2 Abbreviated terms 22
4 Technical reports 23
4.1 Correlation between measurements made with apparatus having characteristics differing from CISPR characteristics and measurements made with CISPR apparatus 23
4.1.1 General 23
4.1.2 Critical interference-measuring instrument parameters 23
4.1.3 Impulse interference – correlation factors 25
4.1.4 Random noise 27
4.1.5 The root mean square (RMS) detector 27
4.1.6 Discussion 27
4.1.7 Application to typical noise sources 27
4.1.8 Conclusions 28
4.2 Interference simulators 29
4.2.1 General 29
4.2.2 Types of interference signals 29
4.2.3 Circuits for simulating broadband interference 30
4.3 Relationship between limits for open-area test site and the reverberation chamber 34
4.3.1 General 34
4.3.2 Correlation between measurement results of the reverberation chamber and OATS 34
4.3.3 Limits for use with the reverberation chamber method 35
4.3.4 Procedure for the determination of the reverberation chamber limit 35
4.4 Characterization and classification of the asymmetrical disturbance source induced in telephone subscriber lines by AM broadcasting transmitters in the LW, MW and SW bands 36
4.4.1 General 36
4.4.2 Experimental characterization 36
4.4.3 Prediction models and classification 46
4.4.4 Characterization of the immunity-test disturbance source 50
4.5 Predictability of radiation in vertical directions at frequencies above 30 MHz 57
4.5.1 Summary 57
4.5.2 Range of application 58
4.5.3 General 58
4.5.4 Method used to calculate field patterns in the vertical plane 60
4.5.5 Limitations of predictability of radiation at elevated angles 61
4.5.6 Differences between the fields over a real ground and the fields over a perfect conductor 89
4.5.7 Uncertainty ranges 95
4.5.8 Conclusions 97

Documents
Document Sharing Hub
Full document details: PD CISPR TR 16-3:2020

4.6 The predictability of radiation in vertical directions at frequencies up to 30 MHz 98
4.6.1 Range of application 98
4.6.2 General 99
4.6.3 Method of calculation of the vertical radiation patterns 100
4.6.4 The source models 100
4.6.5 Electrical constants of the ground 102
4.6.6 Predictability of radiation in vertical directions 102
4.6.7 Conclusions 110
4.6.8 Figures associated with predictability of radiation in vertical directions 111
4.7 Correlation between amplitude probability distribution (APD) characteristics of disturbance and performance of digital communication systems 146
4.7.1 General 146
4.7.2 Influence on a wireless LAN system 146
4.7.3 Influence on a Bluetooth system 149
4.7.4 Influence on a W-CDMA system 153
4.7.5 Influence on Personal Handy Phone System (PHS) 156
4.7.6 Quantitative correlation between noise parameters and system performance 160
4.7.7 Quantitative correlation between noise parameters of repetition pulse and system performance of PHS and W-CDMA (BER) 163
4.8 Background material on the definition of the RMS-average weighting detector for measuring receivers 166
4.8.1 General – purpose of weighted measurement of disturbance 166
4.8.2 General principle of weighting – the CISPR quasi-peak detector 167
4.8.3 Other detectors defined in CISPR 16-1-1 167
4.8.4 Procedures for measuring pulse weighting characteristics of digital radiocommunications services 168
4.8.5 Theoretical studies 171
4.8.6 Experimental results 173
4.8.7 Effects of spread-spectrum clock interference on wideband radiocommunication signal reception 191
4.8.8 Analysis of the various weighting characteristics and proposal of a weighting detector 192
4.8.9 Properties of the RMS-average weighting detector 194
4.9 Common mode absorption devices (CMAD) 196
4.9.1 General 196
4.9.2 CMAD as a two-port device 198
4.9.3 Measurement of CMAD 202
4.10 Background on the definition of the FFT-based receiver 212
4.10.1 General 212
4.10.2 Tuned selective voltmeters and spectrum analyzers 213
4.10.3 General principle of a tuned selective voltmeter 213
4.10.4 FFT-based receivers – digital signal processing 214
4.10.5 Measurement errors specific to FFT processing 218
4.10.6 FFT-based receivers – examples 220
4.11 Parameters of signals at telecommunication ports 233
4.11.1 General 233
4.11.2 Estimation of common mode disturbance levels 234
4.12 Background on CDNE equipment and measurement method 235

AVA Documents
Document Sharing Hub
Full document details: PD CISPR TR 16-3:2020

4.12.1 General ... 235
4.12.2 Historical overview ... 236
4.12.3 From CDN to CDNE ... 240
4.13 Background on LLAS, validation and measurement method ... 243
4.13.1 General ... 243
4.13.2 Historical overview ... 243
4.13.3 Models and equations for the LLAS method ... 244
5 Background and history of CISPR ... 244
5.1 The history of CISPR ... 244
5.1.1 The early years: 1934-1984 ... 244
5.1.2 The division of work ... 246
5.1.3 The computer years: 1984 to 1998 ... 247
5.1.4 The people in CISPR ... 247
5.2 Historical background to the method of measurement of the interference power produced by electrical household and similar appliances in the VHF range ... 248
5.2.1 Historical detail ... 248
5.2.2 Development of the method ... 249
Annex A (informative) Derivation of the formula ... 251
Annex B (informative) The field-strength distribution ... 255
B.1 General ... 255
B.2 H_o-field expressions ... 255
B.3 H_i field expressions ... 257
B.4 E_o-field expressions ... 258
Annex C (informative) The induced asymmetrical open-circuit voltage distribution ... 259
C.1 General ... 259
C.2 H-field-based relations ... 259
C.3 E-field-based relations ... 261
Annex D (informative) The outlet-voltage distribution ... 262
D.1 General ... 262
D.2 H-field-based relations ... 262
D.3 E-field-based relations ... 263
Annex E (informative) Some mathematical relations ... 264
E.1 General ... 264
E.2 The error function ... 264
E.3 Application to the lognormal distribution ... 265
Annex F (informative) Harmonic fields radiated at elevated angles from 27 MHz ISM equipment over real ground ... 266
Annex G (informative) Models and equations associated with the LLAS method ... 272
G.1 General ... 272
G.2 Response of an LAS to a magnetic field dipole ... 272
G.2.1 Magnetic field strength model of a disturbance source ... 272
G.2.2 Response of an LAS to a magnetic field dipole ... 273
G.2.3 Sensitivity of an LLAS for different diameters ... 277
G.2.4 Limitation of application of the relative sensitivity curves ... 278
G.3 Response of LLAS to the LLAS verification dipole ... 279
G.3.1 Relation of LLA current and voltage applied to the LLAS verification dipole ... 279

AVA Documents
Document Sharing Hub
Full document details: PD CISPR TR 16-3:2020

G.3.2 Calculation of mutual inductance: the original method 280
G.3.3 Calculation of mutual inductance: the improved method 280
G.3.4 Derivation of the equation for the reference validation factor 280
G.3.5 Replication of the original version of the reference validation factor 283
G.3.6 Calculation of the improved reference validation factor 283
G.3.7 NEC2 method 285
G.4 Magnetic field strength of a magnetic field dipole above a ground plane 286
G.4.1 Model 286
G.4.2 Replication of Figure C.10 287
G.4.3 Conversion factors for calculating magnetic field strength at other distances 289
G.5 LLAS validation criterion 290
Bibliography 291

Figure 1 – Relative response of various detectors to impulse interference 24
Figure 2 – Pulse rectification coefficient $P(\alpha)$ 25
Figure 3 – Pulse repetition frequency 26
Figure 4 – Block diagram and waveforms of a simulator generating noise bursts 32
Figure 5 – Block diagram of a simulator generating noise bursts according to the pulse principle 33
Figure 6 – Details of a typical output stage 34
Figure 7 – Scatter plot of the measured outdoor magnetic field strength H_o (dBμA/m) versus the calculated outdoor magnetic field strength H_c dB(μA/m) 38
Figure 8 – Measured outdoor magnetic versus distance, and probability of the building-effect parameter 39
Figure 9 – Normal probability plot of the building-effect parameter A_b dB 40
Figure 10 – Scatter plot of the outdoor antenna factor G_o dB(Ωm) versus the indoor antenna factor G_i 41
Figure 11 – Normal probability plots of the antenna factors 42
Figure 12 – Normal probability plot of the equivalent asymmetrical resistance R_a dB(Ω) 45
Figure 13 – Examples of the frequency dependence of some parameters 46
Figure 14 – Example of the frequency histogram $\Delta N(E_o,\Delta E_o)$ 51
Figure 15 – Example of $n_m(E_o)$, i.e. the distribution of the outlets experiencing a maximum field strength E_o resulting from a given number of transmitters in (or near) the respective geographical region 52
Figure 16 – Example of the number of outlets with an induced asymmetrical open-circuit voltage $U_L \leq U_h \leq U_{max}$ = 79 V (see Table 10) 54
Figure 17 – Examples of number (left-hand scale) and relative number (right-hand scale) of outlets with $U_L \leq U_h \leq U_{max}$ 55
Figure 18 – Vertical polar patterns of horizontally polarized E_x field strengths emitted around small vertical loop (horizontal magnetic dipole) over three different types of real ground 63
Figure 19 – Height scan patterns of vertically oriented E_z field strengths emitted from small vertical loop (horizontal magnetic dipole) over three different types of real ground 63
Figure 20 – Vertical polar patterns of horizontally polarized E_x field strengths emitted around small vertical loop (horizontal magnetic dipole), over three different types of real ground 65

Documents
Document Sharing Hub
Full document details: PD CISPR TR 16-3:2020

Figure 21 – Vertical polar patterns of vertically oriented E_z field strengths emitted around small vertical loop (horizontal magnetic dipole) over three different types of real ground 65

Figure 22 – Height scan patterns of vertically oriented E_z field strengths emitted at 1 000 MHz from the small vertical loop (horizontal magnetic dipole), at horizontal distance of 10 m, 30 m and 300 m in the Z-X plane over three different types of real ground 66

Figure 23 – Vertical polar patterns of horizontally polarized E_x and vertically oriented E_z field strengths emitted around small horizontal electric dipole, in Y-Z and Z-X planes respectively 68

Figure 24 – Height scan patterns of horizontally polarized E_x field strengths emitted from small horizontal electric dipole 68

Figure 25 – Vertical polar patterns of horizontally polarized E_x and vertically oriented E_z field strengths emitted around small horizontal electric dipole in Y-Z and Z-X planes respectively 71

Figure 26 – Height scan patterns of horizontally polarized E_x field strengths emitted small horizontal electric dipole 71

Figure 27 – Vertical polar patterns of horizontally polarized E_x and vertically oriented E_z field strengths emitted around small vertical loop (horizontal magnetic dipole) in Y-Z and Z-X planes respectively 72

Figure 28 – Height scan patterns of vertically oriented E_z and horizontally oriented E_x field strengths emitted from small vertical loop (horizontal magnetic dipole) 72

Figure 29 – Vertical polar patterns of vertically oriented E_z and horizontally oriented E_x field strengths emitted around small vertical electric dipole 75

Figure 30 – Height scan patterns of vertically oriented E_z and horizontally oriented E_x field strengths emitted from small vertical electric dipole 75

Figure 31 – Vertical polar patterns of horizontally polarized E_x and vertically oriented E_z field strengths emitted around small vertical loop (horizontal magnetic dipole) in Y-Z and Z-X planes respectively 76

Figure 32 – Height scan patterns of vertically oriented E_z and horizontally oriented E_x field strengths emitted from small vertical loop (horizontal magnetic dipole) 76

Figure 33 – Vertical polar patterns of horizontally polarized E-field strength emitted around small horizontal loop (vertical magnetic dipole) 77

Figure 34 – Height scan patterns of horizontally polarized E-field strength emitted from small horizontal loop (vertical magnetic dipole) 77

Figure 35 – Vertical polar patterns of vertically oriented E_z and horizontally oriented E_x field strengths emitted around small vertical electric dipole 80

Figure 36 – Height scan patterns of vertically oriented E_z and horizontally oriented E_x field strengths emitted from the small vertical electric dipole 80

Figure 37 – Vertical polar patterns of horizontally polarized E_x and vertically oriented E_z field strengths emitted around small vertical loop (horizontal magnetic dipole) in Y-Z and Z-X planes respectively 81

Figure 38 – Height scan patterns of vertically oriented E_z and horizontally oriented E_x field strengths emitted from small vertical loop (horizontal magnetic dipole) 81

Figure 39 – Vertical polar patterns of horizontally polarized E-field strength emitted around small horizontal loop (vertical magnetic dipole) 82

Figure 40 – Height scan patterns of horizontally polarized E-field strength emitted from small horizontal loop (vertical magnetic dipole) 82

Figure 41 – Vertical polar patterns of horizontally polarized E-field strength emitted around the small horizontal loop (vertical magnetic dipole) 85

Figure 42 – Height scan patterns of horizontally polarized E-field strength emitted from small horizontal loop (vertical magnetic dipole) 85

AVA Documents
Document Sharing Hub

Full document details: PD CISPR TR 16-3:2020

Figure 43 – Height scan patterns of horizontally polarized E-field strength emitted from small horizontal loop (vertical magnetic dipole) 89

Figure 44 – Height scan patterns of the vertical component of the E-fields emitted from a small vertical electric dipole 92

Figure 45 – Height scan patterns of the vertical component of the E-fields emitted from a small vertical electric dipole 92

Figure 46 – Height scan patterns of the horizontally polarized E-fields emitted in the vertical plane normal to the axis of a small horizontal electric dipole 94

Figure 47 – Height scan patterns of the horizontally polarized E-fields emitted in the vertical plane normal to the axis of a small horizontal electric dipole 94

Figure 48 – Ranges of uncertainties in the predictability of radiation in vertical directions from electrically small sources located at a height of 1 m or 2 m above ground 96

Figure 49 – Ranges of uncertainties in the predictability of radiation in vertical directions from electrically small sources located at a height of 1 m or 2 m above ground 96

Figure 50 – Ranges of uncertainties in the predictability of radiation in vertical directions from electrically small sources located at a height of 1 m or 2 m above ground 97

Figure 51 – Geometry of the small vertical electric dipole model 101

Figure 52 – Geometry of the small horizontal electrical dipole model 101

Figure 53 – Geometry of the small horizontal magnetic dipole model (small vertical loop) 101

Figure 54 – Geometry of the small vertical magnetic dipole model (small horizontal loop) 101

Figure 55 – Ranges of errors in the predictability of radiation in vertical directions from electrically small sources located close to the ground, based on measurements of the horizontally oriented H-field near ground at a distance of 30 m from the sources 109

Figure 56 – Ranges of errors in the predictability of radiation in vertical directions from electrically small sources located close to the ground, based on measurements of the horizontally oriented H-field at the ground supplemented with measurements of the vertically oriented H-field in a height scan up to 6 m at a distance of 30 m from the sources 110

Figure 57 – Vertical radiation patterns of horizontally oriented H-fields emitted by a small vertical electric dipole located close to the ground 112

Figure 58 – Vertical radiation patterns of horizontally oriented H-fields emitted by a small vertical electric dipole located close to the ground 112

Figure 59 – Vertical radiation patterns of E-fields emitted by a small vertical electric dipole located close to the ground 113

Figure 60 – Vertical radiation patterns of the E-fields emitted by a small vertical electric dipole located close to the ground 113

Figure 61 – Vertical radiation patterns of the H-fields emitted by a small horizontal electric dipole located close to the ground 115

Figure 62 – Influence of a wide range of values of the electrical constants of the ground on the vertical radiation patterns of the horizontally oriented H-fields emitted by a small horizontal electric dipole located close to the ground 115

Figure 63 – Vertical radiation patterns of the horizontally oriented H-fields emitted by a small horizontal electric dipole located close to the ground 116

Figure 64 – Vertical radiation patterns of the E-fields emitted by a small horizontal electric dipole located close to the ground 116

Documents
Document Sharing Hub

Full document details: PD CISPR TR 16-3:2020

Figure 65 – Vertical radiation patterns of the E-fields emitted by a small horizontal electric dipole located close to the ground 117
Figure 66 – Vertical radiation patterns of H-fields emitted by small horizontal magnetic dipole (vertical loop) located close to ground 117
Figure 67 – Vertical radiation patterns of the horizontally oriented H-fields emitted by a small horizontal magnetic dipole (vertical loop) located close to the ground 118
Figure 68 – Vertical radiation patterns of the horizontally oriented H-fields emitted by a small horizontal magnetic dipole (vertical loop) located close to the ground 118
Figure 69 – Vertical radiation patterns of the E-fields emitted by a small horizontal magnetic dipole (vertical loop) located close to the ground 119
Figure 70 – Vertical radiation patterns of the E-fields emitted by a small horizontal magnetic dipole (vertical loop) located close to the ground 119
Figure 71 – Vertical radiation patterns of the H-fields emitted by a small vertical magnetic dipole (horizontal loop) located close to the ground 121
Figure 72 – Vertical radiation patterns of the H-fields emitted by a small vertical magnetic dipole (horizontal loop) located close to the ground 121
Figure 73 – Vertical radiation patterns of the H-fields emitted by a small vertical magnetic dipole (horizontal loop) located close to the ground 122
Figure 74 – Vertical radiation patterns of the H-fields emitted by a small vertical magnetic dipole (horizontal loop) located close to the ground 122
Figure 75 – Vertical radiation pattern of the E-field emitted by a small vertical magnetic dipole (horizontal loop) located close to the ground 123
Figure 76 – Vertical radiation patterns of the E-fields emitted by a small vertical magnetic dipole (horizontal loop) located close to the ground 123
Figure 77 – Vertical radiation patterns of the horizontally oriented H-fields emitted by a small vertical electric dipole located close to the ground 124
Figure 78 – Vertical radiation patterns of the E-fields emitted by a small vertical electric dipole located close to the ground 124
Figure 79 – Vertical radiation patterns of the E-fields emitted by a small vertical electric dipole located close to the ground 125
Figure 80 – Vertical radiation patterns of the H-fields emitted by a small horizontal electric dipole located close to the ground 125
Figure 81 – Vertical radiation patterns of the horizontally oriented H-fields emitted by a small horizontal electric dipole located close to the ground 126
Figure 82 – Vertical radiation patterns of the E-fields emitted by a small horizontal electric dipole located close to the ground 126
Figure 83 – Vertical radiation patterns of the E-fields emitted by a small horizontal electric dipole located close to the ground 128
Figure 84 – Vertical radiation patterns of the H-fields emitted by a small horizontal magnetic dipole (vertical loop) located close to the ground 128
Figure 85 – Vertical radiation patterns of the horizontally oriented H-fields emitted by a small horizontal magnetic dipole (vertical loop) located close to the ground 129
Figure 86 – Vertical radiation patterns of the horizontally oriented H-fields emitted by a small horizontal magnetic dipole (vertical loop) located close to the ground 129
Figure 87 – Vertical radiation patterns of the E-fields emitted by a small horizontal magnetic dipole (vertical loop) located close to the ground 130
Figure 88 – Vertical radiation patterns of the E-fields emitted by a small horizontal magnetic dipole (vertical loop) located close to the ground 130
Figure 89 – Vertical radiation patterns of the H-fields emitted by a small vertical magnetic dipole (horizontal loop) located close to the ground 131

AVA Documents
Document Sharing Hub

Full document details: PD CISPR TR 16-3:2020

Figure 90 – Vertical radiation patterns of the H-fields emitted by a small vertical magnetic dipole (horizontal loop) located close to the ground 131
Figure 91 – Vertical radiation patterns of the H-fields emitted by a small vertical magnetic dipole (horizontal loop) located close to the ground 132
Figure 92 – Vertical radiation patterns of the E-fields emitted by a small vertical magnetic dipole (horizontal loop) located close to the ground 132
Figure 93 – Vertical radiation patterns of the horizontally oriented H-fields emitted by a small vertical electric dipole located close to the ground 133
Figure 94 – Vertical radiation patterns of the E-fields emitted by a small vertical electric dipole located close to the ground 133
Figure 95 – Vertical radiation patterns of the E-fields emitted by a small vertical electric dipole located close to the ground 135
Figure 96 – Vertical radiation patterns of the H-fields emitted by a small horizontal electric dipole located close to the ground 135
Figure 97 – Vertical radiation patterns of the E-fields emitted by a small horizontal electric dipole located close to the ground 136
Figure 98 – Vertical radiation patterns of the E-fields emitted by a small horizontal electric dipole located close to the ground 136
Figure 99 – Vertical radiation patterns of the H-field emitted by a small horizontal magnetic dipole (vertical loop) located close to the ground 138
Figure 100 – Vertical radiation patterns of the vertically polarized E-fields emitted by a small horizontal magnetic dipole (vertical loop) located close to the ground 138
Figure 101 – Vertical radiation patterns of the H-field emitted by a small vertical magnetic dipole (horizontal loop) located close to the ground 139
Figure 102 – Vertical radiation patterns of the E-fields emitted by a small vertical magnetic dipole (horizontal loop) located close to the ground 139
Figure 103 – Vertical radiation patterns of the horizontally oriented H-fields emitted by a small vertical electric dipole located close to the ground 140
Figure 104 – Vertical radiation patterns of the vertically polarized E-fields emitted by a small vertical electric dipole located close to the ground 140
Figure 105 – Vertical radiation patterns of the H-fields emitted by a small horizontal electric dipole located close to the ground 141
Figure 106 – Vertical radiation patterns of the horizontally oriented H-fields emitted by a small horizontal electric dipole located close to the ground 141
Figure 107 – Influence of a wide range of values of the electrical constants of the ground on the vertical radiation patterns of the horizontally oriented H-fields emitted by a small horizontal electric dipole located close to the ground 142
Figure 108 – Vertical radiation patterns of the vertically polarized E-fields emitted by a small horizontal electric dipole located close to the ground 142
Figure 109 – Vertical radiation patterns of the H-fields emitted by a small horizontal magnetic dipole (vertical loop) located close to the ground 144
Figure 110 – Vertical radiation patterns of the vertically polarized E-fields emitted by a small horizontal magnetic dipole (vertical loop) located close to the ground 144
Figure 111 – Vertical radiation patterns of the H-fields emitted by a small vertical magnetic dipole (horizontal loop) located close to the ground 145
Figure 112 – Vertical radiation patterns of the E-fields emitted by a small vertical magnetic dipole (horizontal loop) located close to the ground 145
Figure 113 – Set-up for measuring communication quality degradation of a wireless LAN 146
Figure 114 – APD characteristics of disturbance 148
Figure 115 – Wireless LAN throughput influenced by noise 149

AVA Documents
Document Sharing Hub
Full document details: PD CISPR TR 16-3:2020

Figure 116 – Set-up for measuring the communication quality degradation of Bluetooth 150
Figure 117 – APD of disturbance of actual MWO (2 441MHz) 150
Figure 118 – APD characteristics of disturbance (2 460 MHz) 151
Figure 119 – Throughput of Bluetooth influenced by noise 153
Figure 120 – Set-up for measuring the BER of W-CDMA 154
Figure 121 – APD characteristics of disturbance 155
Figure 122 – BER of W-CDMA caused by radiation noise 156
Figure 123 – Set-up for measuring the PHS throughput 157
Figure 124 – Set-up for measuring the BER of PHS 157
Figure 125 – APD characteristics of disturbance 158
Figure 126 – PHS throughput caused by radiation 159
Figure 127 – BER of PHS caused by radiation noise 160
Figure 128 – Correlation of the disturbance voltages with the system performance (C/N_0) 161
Figure 129 – Correlation of the disturbance voltages with the system performance 161
Figure 130 – Correlation of the disturbance voltages with the system performance 162
Figure 131 – Correlation of the disturbance voltages with the system performance (C/N_0) 162
Figure 132 – Correlation of the disturbance voltages with the system performance (C/N_0) 163
Figure 133 – Experimental set-up for measuring communication quality degradation of a PHS or W-CDMA 163
Figure 134 – Simulation set-up for estimating communication quality degradation of a PHS or W-CDMA 164
Figure 135 – APD of pulse disturbance 164
Figure 136 – BER degradation of PHS and W-CDMA caused by repetition pulse (Carrier power, –35 dBm) 165
Figure 137 – Evaluation method of the correlation between BER and APD 165
Figure 138 – Correlation between measured ΔL_{BER} and ΔL_{APD} 166
Figure 139 – Correlation between measured p_{BER} and p_{APD} 166
Figure 140 – Weighting curves of quasi-peak measuring receivers for the different frequency ranges as defined in CISPR 16-1-1 167
Figure 141 – Weighting curves for peak, quasi-peak, RMS and linear average detectors for CISPR bands C and D 168
Figure 142 – Test setup for the measurement of the pulse weighting characteristics of a digital radiocommunication system 169
Figure 143 – Example of an interference spectrum: pulse modulated carrier with a pulse duration of 0,2 μs and a PRF < 10 kHz 170
Figure 144 – The RMS and peak levels for constant BEP for three K = 3, convolutional codes of different rate 172
Figure 145 – The RMS and peak levels for constant BEP for two rate ½, convolutional code 173
Figure 146 – Test setup for the measurement of weighting curves for Digital Radio Mondiale (DRM) 175
Figure 147 – Weighting characteristics for DRM signals for various pulse widths of the pulse-modulated carrier 176

Documents
Document Sharing Hub
Full document details: PD CISPR TR 16-3:2020

Figure 148 – Weighting characteristics for DRM protection level 0: average of results for two receivers 177
Figure 149 – Weighting characteristics for DRM protection level 1: average of results for two receivers 177
Figure 150 – Weighting characteristics for DVB-T with 64 QAM 2k, *CR* 3/4 (as used in France and UK) 179
Figure 151 – Weighting characteristics for DVB-T with 64 QAM 8k, *CR* 3/4 (as used in Spain) 180
Figure 152 – Weighting characteristics for DVB-T with 16 QAM 8k, *CR* 2/3 (as used in Germany) 180
Figure 153 – Average weighting characteristics of 6 receiver types for DVB-T with 16QAM 181
Figure 154 – Average weighting characteristics of 6 receiver types for DVB-T with 64QAM 181
Figure 155 – Weighting characteristics for DAB (signal level -71 dBm) with a flat response down to approximately 1 kHz 182
Figure 156 – Weighting characteristics for DAB: average of two different commercial receiver types 183
Figure 157 – Weighting characteristics for TETRA (signal level – 80 dBm) for a code rate of 1 184
Figure 158 – Weighting characteristics for RBER 1b of GSM (signal level –90 dBm) 185
Figure 159 – Weighting characteristics for RBER 2 of GSM 185
Figure 160 – Carrier-to-interference improvements with decreasing PRF in dB computed for GSM using COSSAP 186
Figure 161 – RMS and quasi-peak values of pulse level for constant effect on FM radio reception 186
Figure 162 – Weighting characteristics for RBER 1b of GSM (signal level –90 dBm) 187
Figure 163 – Weighting characteristics for DECT (signal level –83 dBm) 188
Figure 164 – Weighting characteristics for IS-95 (signal level -97 dBm) with comparatively high immunity to interference 189
Figure 165 – Weighting characteristics for J-STD 008 (signal level –97 dBm) 189
Figure 166 – Weighting characteristics for the Frame Error Ratio (FER) of CDMA2000 (measured at a receive signal level of –112 dBm) for a low data rate of 9,6 kb/s 190
Figure 167 – Weighting characteristics for the Frame Error Ratio (FER) of CDMA2000 (measured at a receive signal level of –106 dBm) for two different data rates (9,6 kb/s and 76,8 kb/s) 190
Figure 168 – The proposed RMS-average detector for CISPR Bands C and D with a corner frequency of 100 Hz 193
Figure 169 – RMS-average detector function by using an RMS detector followed by a linear average detector and peak reading 193
Figure 170 – RMS-average weighting functions for CISPR Bands A, B, C/D and E for the shortest pulse widths allowed by the measurement bandwidths 194
Figure 171 – Shift of the RMS-average weighting function for CISPR band C/D by using a bandwidth of 1 MHz instead of 120 kHz, if the shortest possible pulse widths are applied 195
Figure 172 – Example of a simple EUT model 197
Figure 173 – Representation of a CMAD as a two-port device 198
Figure 174 – Conformal mapping between z-plane and f-plane 201

Documents
Document Sharing Hub
Full document details: PD CISPR TR 16-3:2020

Figure 175 – Conversion from 50 Ω coaxial system to the geometry of the two-port device-under-test 203
Figure 176 – Basic model for the TRL calibration 204
Figure 177 – The four calibration configurations necessary for the TRL calibration 205
Figure 178 – Measurement of CMAD characteristics 209
Figure 179 – Preliminary measurements of the test set-up 211
Figure 180 – Position of the reference planes for the measurement with SOLT calibration and $ABCD$ transformation to Z_{ref} level 212
Figure 181 – Superheterodyne EMI receiver 214
Figure 182 – An example spectrogram $Z[m,k]$ 216
Figure 183 – Sidelobe effect due to the finite length of window 218
Figure 184 – Measurement error for a single pulse 219
Figure 185 – IF signal for different overlapping factors for the same sequence of pulses 220
Figure 186 – FFT-based baseband system 221
Figure 187 – Real-time FFT-based measuring instrument 222
Figure 188 – Digital down-converter 222
Figure 189 – Short time fast Fourier transform – An example of implementation 223
Figure 190 – Floating-point analogue-to-digital conversion 223
Figure 191 – Example of a 120 kHz Gaussian filter 224
Figure 192 – Essential parts of an FFT-based heterodyne receiver 225
Figure 193 – Dynamic range for broadband emission as measured with the peak detector 227
Figure 194 – Set-up of FFT-based system type 2 227
Figure 195 – FFT Software (“FFTemi”) screen shot 230
Figure 196 – Example of pulse generator measurement with antenna 231
Figure 197 – Radiated emission measurement of a motor – peak detector 231
Figure 198 – Angular characterization of a PC 232
Figure 199 – Example FFT IF analysis display 233
Figure 200 – Equivalent radiated measurement methods (30 MHz to 300 MHz) 237
Figure 201 – Measured relationship between field strength E_{z} and CM current I_{cm} for various termination resistances R 237
Figure 202 – Modelled relationship between field strength E_{z} and CM current I_{cm} using EUT height 0,8 m, measurement distance 3 m, receive antenna height 1 m 239
Figure 203 – Limit for the terminal voltage at the CDN 239
Figure 204 – Results of a Philips 11-lab internal CDN RRT using an artificial class 1 EUT – expanded uncertainty nearly 10 dB 241
Figure 205 – Block diagram for CDNE-measurement method 242
Figure A.1 – Example plot using the expression $P_{\mathrm{t}} + G = P_{\mathrm{q}} + 2$ 252
Figure A.2 – Examples of a number of microwaves measured for P_{q} and P_{t} 254
Figure B.1 – Definition of the ring-shaped area round the transmitter T 256
Figure C.1 – The permissible ranges of U_{h} and G are within the polygon $\{G_{\mathrm{L}}, U_{\mathrm{a}}\}$, $\{G_{\mathrm{L}}, U_{\mathrm{b}}\}$, $\{G_{\mathrm{U}}, U_{\mathrm{d}}\}$, $\{G_{\mathrm{l}}, U_{\mathrm{c}}\}$ and $\{G_{\mathrm{L}}, U_{\mathrm{a}}\}$. For the given value U_{L} the double-shaded area represents $pr\{U_{\mathrm{h}} \geq U_{\mathrm{L}}\}$ 260

Documents
Document Sharing Hub
Full document details: PD CISPR TR 16-3:2020

Figure F.1 – Vertical radiation patterns of horizontally polarized fields, 109 MHz, 300 m scan radius (adapted from [34]) 268
Figure F.2 – Vertical radiation patterns of horizontally polarized fields, 109 MHz, 300 m scan radius (adapted from [34]) 269
Figure F.3 – Vertical radiation patterns of horizontally polarized fields, 109 MHz, 300 m scan radius (adapted from [34]) 270
Figure F.4 – Vertical radiation patterns of horizontally polarized fields, 109 MHz, 300 m scan radius (adapted from [34]) 271
Figure G.1 – Geometry and coordination system for a single magnetic field dipole 272
Figure G.2 – Configuration of measurement of an EUT in an LLA with two slits 273
Figure G.3 – Transformer model representation of a disturbance source inside an LLA 274
Figure G.4 – Transfer functions $f_c(\omega)$, $g_c(\omega)$ and their product (expressed in dB) as a function of frequency for a 2 m LLAS 277
Figure G.5 – Sensitivity S_D of an LLAS with diameter D relative to an LLAS with 2 m diameter (Figure C.11 of CISPR 16-1-4:2019 [102]) 278
Figure G.6 – Setup of the LLAS verification dipole for verification of an LLAS 279
Figure G.7 – Geometry model of LLA for numerical computation of Neumann integral [113] 282
Figure G.8 – LLAS verification dipole excluding the coupling effect from the LLAS loops 282
Figure G.9 – Network model representation of the LLAS verification dipole fed by a generator source and the LLA 283
Figure G.10 – First version of the reference validation factor for an LLA of 2 m diameter (Figure C.8 of CISPR 16-1-4:2010 [102]) 283
Figure G.11 – Reference validation factors for an LLA of 2 m, 3 m and 4 m diameter (Figure C.8 of CISPR 16-1-4:2019 and CISPR 16-1-4:2019/AMD1:2020 [102]) 284
Figure G.12 – Relative sensitivities of the LLAS verification dipole for an LLAS with different diameters (relative to an LLAS of 2 m diameter) 285
Figure G.13 – Comparison of analytical and numerical (NEC2) calculations of the reference validation factors 285
Figure G.14 – Magnetic field dipole moment of a small loop radiator in free space 287
Figure G.15 – EUT above a ground plane and the coordinate system and possible magnetic field dipole orientations 287
Figure G.16 – Magnetic field strength resulting from a source and its image below the ground plane (side view) 287
Figure G.17 – Magnetic field strength expressed in dB(μA/m) of three magnetic field dipole orientations at three distances 288
Figure G.18 – Conversion factors C_{dA} [for conversion into dB(μA/m)] for three standard measurement distances d (replicated Figure C.10 of CISPR 16-1-4:2010; exclusive the 30 m curve [102]) 289
Figure G.19 – Conversion factors for calculating magnetic field strength at 10 m or 30 m ... 289

Table 1 – Comparative response of slideback peak, quasi-peak and average detectors to sine wave, periodic pulse and Gaussian waveform 24
Table 2 – Characteristics of gate generator and modulator to simulate various types of broadband interference 30
Table 3 – Summary results of building-effect, A_b, analysis 40
Table 4 – Summary of results of G-factor analysis 43
Table 5 – Summary of L_o factors (far-field) 44

AVA Documents
Document Sharing Hub
Full document details: PD CISPR TR 16-3:2020

Table 6 – Summary of truncation parameters of $f(G)$ 44
Table 7 – Summary results of equivalent-resistance analysis 45
Table 8 – Example of field-strength classification 48
Table 9 – Example of voltage classification assuming for the outdoor field strength: E_{max} = 60 V/m and E_{min} = 0,01 V/m 49
Table 10 – Summary of the parameters used in the numerical examples presented in Figure 16 and Figure 17 53
Table 11 – Frequencies of interest in ITU designated bands from Table 9 of CISPR 11:2009 60
Table 12 – Electrical constants for “medium dry ground” [31] (CCIR: medium dry ground; rocks; sand; medium sized towns[32]) 61
Table 13 – Electrical constants for “wet ground” [31] (CCIR: marshes (fresh water); cultivated land [24]) and “very dry ground” [31] (CCIR: very dry ground; granite mountains in cold regions; industrial areas [32]) 61
Table 14 – Estimates of the errors in prediction of radiation in vertical directions based on a measurement height scan from 1 m to 4 m at known distances, d; frequency = 75 MHz (adapted from [39]) 69
Table 15 – Estimates of the errors in prediction of radiation in vertical directions based on a measurement height scan from 1 m to 4 m at known distances, d; frequency = 110 MHz (adapted from [39]) 73
Table 16 – Estimates of the errors in prediction of radiation in vertical directions based on a measurement height scan from 1 m to 4 m at known distances, d; frequency = 243 MHz (adapted from [39]) 78
Table 17 – Estimates of the errors in prediction of radiation in vertical directions based on a measurement height scan from 1 m to 4 m at known distances, d; frequency = 330 MHz (adapted from [39]) 83
Table 18 – Estimates of the errors in prediction of radiation in vertical directions based on a measurement height scan from 1 m to 4 m at known distances, d; frequency = 1 000 MHz (adapted from [39]) 86
Table 19 – Predictability of radiation in vertical directions at 100 kHz, using ground-based measurements of horizontally oriented H-field at distances up to 3 km from the source (figures are located in 4.6.8) 103
Table 20 – Predictability of radiation in vertical directions at 1 MHz, using ground-based measurements of horizontally oriented H-field at distances up to 300 m from the source (figures are located in 4.6.8) 104
Table 21 – Predictability of radiation in vertical directions at 10 MHz, using ground-based measurements of horizontally oriented H-field at distances up to 300 m from the source (figures are located in 4.6.8) 105
Table 22 – Predictability of radiation in vertical directions at 30 MHz, using ground-based measurements of horizontally oriented H-field at distances up to 300 m from the source (figures are located in 4.6.8) 106
Table 23 – Conditions for measuring communication quality degradation 147
Table 24 – Average and RMS values of noise level normalized by N_0 148
Table 25 – Conditions for measuring communication quality degradation of Bluetooth 150
Table 26 – Average and RMS values of noise level normalized by N_0 151
Table 27 – Average and RMS values of noise level normalized by N_0 152
Table 28 – Conditions for measuring communication quality degradation of W-CDMA 154
Table 29 – Average and RMS values of noise level normalized by N_0 155
Table 30 – Conditions for measuring the PHS throughput 157
Table 31 – Conditions for measuring the BER of PHS 157

AVA Documents
Document Sharing Hub
Full document details: PD CISPR TR 16-3:2020

Table 32 – Average and RMS values of noise level normalized by N_0 158
Table 33 – Overview of types of interference used in the experimental study of weighting characteristics 170
Table 34 – DRM radio stations received for the measurement of the weighting characteristics 174
Table 35 – Comparison of BER values for the same interference level 178
Table 36 – Transmission parameters of DVB-T systems used in various countries 179
Table 37 – Example of measurement results in dB(μV) of unmodulated and FM modulated carriers for various detectors (bandwidth 120 kHz) 191
Table 38 – Survey of the corner frequencies found in the various measurement results 192
Table 39 – Measurement results for broadband disturbance sources (measurements with RMS-average and quasi-peak detectors are normalized to average detector values) 196
Table 40 – Expected deviations between different laboratories for small EUTs due to variations of the impedance Z_{apparent} at point B 197
Table 41 – Calibration measurement results format 206
Table 42 – Scan times 224
Table 43 – Sampling rates for different B_{WIF} 228
Table 44 – Scan times for a scan 30 MHz to 1 GHz 229

Documents
Document Sharing Hub
Full document details: PD CISPR TR 16-3:2020

INTERNATIONAL ELECTROTECHNICAL COMMISSION

SPECIFICATION FOR RADIO DISTURBANCE AND IMMUNITY MEASURING APPARATUS AND METHODS –

Part 3: CISPR technical reports

FOREWORD

1) The International Electrotechnical Commission (IEC) is a worldwide organization for standardization comprising all national electrotechnical committees (IEC National Committees). The object of IEC is to promote international co-operation on all questions concerning standardization in the electrical and electronic fields. To this end and in addition to other activities, IEC publishes International Standards, Technical Specifications, Technical Reports, Publicly Available Specifications (PAS) and Guides (hereafter referred to as "IEC Publication(s)"). Their preparation is entrusted to technical committees; any IEC National Committee interested in the subject dealt with may participate in this preparatory work. International, governmental and non-governmental organizations liaising with the IEC also participate in this preparation. IEC collaborates closely with the International Organization for Standardization (ISO) in accordance with conditions determined by agreement between the two organizations.
2) The formal decisions or agreements of IEC on technical matters express, as nearly as possible, an international consensus of opinion on the relevant subjects since each technical committee has representation from all interested IEC National Committees.
3) IEC Publications have the form of recommendations for international use and are accepted by IEC National Committees in that sense. While all reasonable efforts are made to ensure that the technical content of IEC Publications is accurate, IEC cannot be held responsible for the way in which they are used or for any misinterpretation by any end user.
4) In order to promote international uniformity, IEC National Committees undertake to apply IEC Publications transparently to the maximum extent possible in their national and regional publications. Any divergence between any IEC Publication and the corresponding national or regional publication shall be clearly indicated in the latter.
5) IEC itself does not provide any attestation of conformity. Independent certification bodies provide conformity assessment services and, in some areas, access to IEC marks of conformity. IEC is not responsible for any services carried out by independent certification bodies.
6) All users should ensure that they have the latest edition of this publication.
7) No liability shall attach to IEC or its directors, employees, servants or agents including individual experts and members of its technical committees and IEC National Committees for any personal injury, property damage or other damage of any nature whatsoever, whether direct or indirect, or for costs (including legal fees) and expenses arising out of the publication, use of, or reliance upon, this IEC Publication or any other IEC Publications.
8) Attention is drawn to the Normative references cited in this publication. Use of the referenced publications is indispensable for the correct application of this publication.
9) Attention is drawn to the possibility that some of the elements of this IEC Publication may be the subject of patent rights. IEC shall not be held responsible for identifying any or all such patent rights.

The main task of IEC technical committees is to prepare International Standards. However, a technical committee may propose the publication of a technical report when it has collected data of a different kind from that which is normally published as an International Standard, for example "state of the art."

CISPR 16-3, which is a Technical Report, has been prepared by CISPR subcommittee A: Radio-interference measurements and statistical methods.

This fourth edition cancels and replaces the third edition published in 2015. This edition constitutes a technical revision.

The main technical change with respect to the previous edition consists of the addition of detailed background information on the large loop antenna system (LLAS) and its measurement method in general and on the models and equations which apply to calculate the reference validation factor and conversion factor curves.

AVA Documents
Document Sharing Hub

The text of this Technical Report is based on the following documents:

Draft TR	Report on voting
CIS/A/1298/DTR	CIS/A/1310/RVDTR

Full information on the voting for the approval of this Technical Report can be found in the report on voting indicated in the above table.

This publication has been drafted in accordance with the ISO/IEC Directives, Part 2.

A list of all parts of the CISPR 16 series can be found, under the general title *Specification for radio disturbance and immunity measuring apparatus and methods*, on the IEC website.

The committee has decided that the contents of the base publication and its amendments will remain unchanged until the stability date indicated on the IEC web site under "http://webstore.iec.ch" in the data related to the specific publication. At this date, the publication will be

- reconfirmed,
- withdrawn,
- replaced by a revised edition, or
- amended.

IMPORTANT – The 'colour inside' logo on the cover page of this publication indicates that it contains colours which are considered to be useful for the correct understanding of its contents. Users should therefore print this document using a colour printer.

Documents
Document Sharing Hub

Full document details: PD CISPR TR 16-3:2020

SPECIFICATION FOR RADIO DISTURBANCE AND IMMUNITY MEASURING APPARATUS AND METHODS –

Part 3: CISPR technical reports

1 Scope

This part of CISPR 16 is a collection of technical reports (Clause 4) that serve as background and supporting information for the various other standards and technical reports in CISPR 16 series. In addition, background information is provided on the history of CISPR, as well as a historical reference on the measurement of interference power from household and similar appliances in the VHF range (Clause 5).

Over the years, CISPR prepared a number of recommendations and reports that have significant technical merit but were not generally available. Reports and recommendations were for some time published in CISPR 7 and CISPR 8.

At its meeting in Campinas, Brazil, in 1988, CISPR subcommittee A agreed on the table of contents of CISPR 16-3, and to publish the reports for posterity by giving the reports a permanent place in CISPR 16-3.

With the reorganization of CISPR 16 in 2003, the significance of CISPR limits material was moved to CISPR 16-4-3, whereas recommendations on statistics of disturbance complaints and on the report on the determination of limits were moved to CISPR 16-4-4:2007. The contents of Amendment 1 (2002) of CISPR 16-3:2000 were moved to CISPR 16-4-1.

NOTE As a consolidated collection of independent technical reports, this document can contain symbols that have differing meanings from one clause to the next. Attempts have been made to minimize this to the extent possible at the time of editing.

2 Normative references

The following documents are referred to in the text in such a way that some or all of their content constitutes requirements of this document. For dated references, only the edition cited applies. For undated references, the latest edition of the referenced document (including any amendments) applies.

CISPR 11:2009, *Industrial, scientific and medical equipment – Radio-frequency disturbance characteristics – Limits and methods of measurement*[1]

CISPR 16-1-1, *Specification for radio disturbance and immunity measuring apparatus and methods – Part 1-1: Radio disturbance and immunity measuring apparatus – Measuring apparatus*

IEC 60050-161:1990, *International Electrotechnical Vocabulary (IEV) – Part 161: Electromagnetic compatibility*

[1] 5th edition (2009). This 5th edition has been replaced in 2016 by a 6th Edition CISPR 11, Industrial, scientific and medical equipment – Radio-frequency disturbance characteristics – Limits and methods of measurement.

AVA Documents
Document Sharing Hub
Full document details: PD CISPR TR 16-3:2020

IEC 60050-300:2001, *International Electrotechnical Vocabulary (IEV) – Electrical and electronic measurements and measuring instruments – Part 311: General terms relating to measurements – Part 312: General terms relating to electrical measurements – Part 313: Types of electrical measuring instruments – Part 314: Specific terms according to the type of instrument*

ISO/IEC Guide 99:2007, *International vocabulary of metrology – Basic and general concepts and associated terms (VIM)*

3 Terms, definitions and abbreviated terms

3.1 Terms and definitions

For the purposes of this document, the terms and definitions given in IEC 60050-161, IEC 60050-300, ISO/IEC Guide 99, as well as the following apply.

NOTE While the symbol U is commonly used in CISPR publications to represent uncertainty, in this technical report the symbols U and V are used interchangeably to represent "voltage" in order to accommodate the legacy diagrams contained herein.

3.1.1
asymmetric voltage
radio-frequency disturbance voltage appearing between the electrical mid-point of the mains terminals and earth

Note 1 to entry: It is sometimes called the common-mode voltage and is half the vector sum of V_a and V_b, i.e. $(V_a + V_b)/2$

Note 2 to entry: V_a is the vector voltage between one of the mains terminals and earth, and V_b is the vector voltage between the other mains terminal and earth.

3.1.2
bandwidth
B_n
width of the overall selectivity curve of the receiver between two points at a stated attenuation, below the mid-band response

Note 1 to entry: The bandwidth is represented by the symbol B_n, where n is the stated attenuation in decibels.

3.1.3
electrical charge time constant
T_C
time needed after the instantaneous application of a constant sine-wave voltage to the stage immediately preceding the input of the detector for the output voltage of the detector to reach 63 % of its final value

Note 1 to entry: This time constant is determined as follows. A sine-wave signal of constant amplitude and having a frequency equal to the mid-band frequency of the IF amplifier is applied to the input of the stage immediately preceding the detector. The indication α_{max} of an instrument having no inertia (for example, a cathode-ray oscilloscope) connected to a terminal in the DC amplifier circuit so as not to affect the behaviour of the detector, is noted. The level of the signal is chosen such that the response of the stages concerned remains within the linear operating range. A sine-wave signal of this level, applied for a limited time only and having a wave train of rectangular envelope is gated such that the deflection registered is $0{,}63\alpha_{max}$. The duration of this signal is equal to the charge time of the detector.

3.1.4
electrical discharge time constant
T_D
time needed after the instantaneous removal of a constant sine-wave voltage applied to the stage immediately preceding the input of the detector for the output of the detector to fall to 37 % of its initial value

Documents
Document Sharing Hub
Full document details: PD CISPR TR 16-3:2020

Note 1 to entry: The method of measurement is analogous to that for the charge time constant, but instead of a signal being applied for a limited time, the signal is interrupted for a definite time. The time taken for the deflection to fall to 0,37D is the discharge time constant of the detector.

3.1.5
impulse bandwidth
B_{imp}

$$B_{\text{imp}} = \frac{A(t)_{\text{max}}}{2G_{\text{o}} \times A_{\text{imp}}} \tag{1}$$

where

$A(t)_{\text{max}}$ is the peak of the envelope at the IF output of the receiver with an impulse area A_{imp} applied at the receiver input;

G_{o} is the gain of the circuit at the centre frequency;

specifically, for two critically coupled tuned transformers,

$$B_{\text{imp}} = 1{,}05 \times B_6 = 1{,}31 \times B_3 \tag{2}$$

where B_6 and B_3 are respectively the bandwidths at the –6 dB and –3 dB points (see CISPR 16-1-1 for further information)

3.1.6
impulse area
impulse strength
A_{imp}
voltage-time area of a pulse defined by the integral:

$$A_{\text{imp}} = \int_{-\infty}^{+\infty} V(t)dt \text{ expressed in } \mu\text{Vs or dB}(\mu\text{Vs}) \tag{3}$$

Note 1 to entry: Spectral density D is related to impulse area and is expressed in μV/MHz or dB(μV)/MHz. For rectangular impulses of pulse duration T at frequencies $f \ll 1/T$, the relationship $D = 2 \times 10^6 / A_{\text{imp}}$ applies because D is calibrated in RMS values of a corresponding sine wave.

3.1.7
mechanical time constant of a critically damped indicating instrument
T_{M}

$$T_{\text{M}} = \frac{T_{\text{L}}}{2\pi} \tag{4}$$

where T_{L} is the period of free oscillation of the instrument with all damping removed

Note 1 to entry: For a critically damped instrument, the equation of motion of the system may be written as

$$T_{\text{M}}^2\left(\frac{d^2\alpha}{dt^2}\right) + 2T_{\text{M}}\frac{d\alpha}{dt} + \alpha = ki \tag{5}$$

where

α is the deflection;

i is the current through the instrument;

k is a constant.

It can be deduced from this relation that this time constant is also equal to the duration of a rectangular pulse (of constant amplitude) that produces a deflection equal to 35 % of the steady deflection produced by a continuous current having the same amplitude as that of the rectangular pulse.

AVA Documents
Document Sharing Hub

Note 2 to entry: The methods of measurement and adjustment are deduced from one of the following:

a) The period of free oscillation having been adjusted to $2\pi T_M$, damping is added so that α_{TM} = 0,35 α_{max}.

b) When the period of oscillation cannot be measured, the damping is adjusted to be just below critical such that the over-swing is not greater than 5 % and the moment of inertia of the movement is such that α_{TM} = 0,35 α_{max}.

3.1.8
overload factor
ratio of the level that corresponds to the range of practical linear function of a circuit (or a group of circuits) to the level that corresponds to full-scale deflection of the indicating instrument

Note 1 to entry: The maximum level at which the steady-state response of a circuit (or group of circuits) does not depart by more than 1 dB from ideal linearity defines the range of practical linear function of the circuit (or group of circuits).

3.1.9
symmetric voltage
radio-frequency disturbance voltage appearing between the wires of a two-wire circuit, such as a single-phase mains supply

Note 1 to entry: Symmetric voltage is sometimes called the differential mode voltage and is the vector difference between V_a and V_b, i.e. (V_a – V_b). Refer to the NOTE in 3.1.1 for definition of V_a and V_b.

3.1.10
unsymmetric voltage
amplitude of the vector voltage, V_a or V_b

Note 1 to entry: Unsymmetric voltage is the voltage measured by the use of an artificial mains V-network. Refer to the NOTE in 3.1.1 for definition of V_a and V_b.

3.1.11
weighting (of e.g. impulsive disturbance)
pulse-repetition-frequency (PRF) dependent conversion (mostly reduction) of a peak-detected impulse voltage level to an indication that corresponds to the interference effect on radio reception

Note 1 to entry: For the analogue receiver, the psychophysical annoyance of the interference is a subjective quantity (audible or visual, usually not a certain number of misunderstandings of a spoken text).

Note 2 to entry: For the digital receiver, the interference effect is an objective quantity that may be defined by the critical bit error ratio (BER) or bit error probability (BEP) for which perfect error correction can still occur, or by another objective and reproducible parameter.

3.1.11.1
weighted disturbance measurement
measurement of disturbance using a weighting detector

3.1.11.2
weighting characteristic
peak voltage level as a function of PRF for a constant effect on a specific radiocommunication system, i.e. the disturbance is weighted by the radiocommunication system itself

3.1.11.3
weighting detector
detector which provides an agreed weighting function

3.1.11.4
weighting factor
value of the weighting function relative to a reference PRF or relative to the peak value

Note 1 to entry: Weighting factor is expressed in dB.

Documents
Document Sharing Hub
Full document details: PD CISPR TR 16-3:2020

3.1.11.5
weighting function
weighting curve
relationship between input peak voltage level and PRF for constant level indication of a measuring receiver with a weighting detector, i.e. the curve of response of a measuring receiver to repeated pulses

3.2 Abbreviated terms

ADPCM	Adaptive differential pulse code modulation
AGC	Automatic gain control
AM	Amplitude modulation
AMN	Artificial mains network
APD	Amplitude probability distribution
BEP	Bit error probability
BER	Bit error rate
CDN	Coupling decoupling network
CDNE	CDN for emission measurement
CM	Common mode
CMAD	Common mode absorption device
COFDM	Coded orthogonal frequency division multiplex
DAB	Digital audio broadcasting
DDC	Digital down-conversion
DECT	Digitally enhanced cordless telephone
DIF	Decimated in frequency
DIT	Decimated in time
DM	Differential mode
DPCH	Dedicated physical channel
DPDCH	Dedicated physical data channel
DQPSK	Digital QPSK
DRM	Digital radio mondiale
DVB-T	Digital video broadcasting – terrestrial
EMC	Electromagnetic compatibility
EMI	Electromagnetic emissions
ERP	Equivalent radiating power
EUT	Equipment under test
FER	Frame error rate
FFT	Fast Fourier transform
FM	Frequency modulation
GSM	Global system for mobile communications
GMSK	Gaussian minimum shift keying
GTEM	Gighertz TEM
IF	Intermediate frequency
ILS	Instrument landing system

ISM	Industrial, scientific and medical
ITU	International Telecommunications Union
LAN	Local area network
LAS	Loop antenna system
LCL	Longitudinal conversion loss
LISN	Line-impedance stabilization network
LLA	Large loop antenna
LLAS	Large loop antenna system
LW	Long wave
MPEG	Moving picture expert group
MW	Medium wave
MWO	Microwave oven
OATS	Open-area test site
OFDM	Orthogonal frequency division multiplex
PC	Personal computer
PHS	Personal handy phone system
PRBS	Pseudo random binary sequence
PRF	Pulse-repetition frequency
QAM	Quadrature amplitude modulation
QPSK	Quadrature phase-shift keying
RAM	Random access memory
RBER	Residual bit error rate
RF	Radio frequency
RMS	Root-mean square
RRT	Round robin test
RSA	Ring-shaped area
SAC	Semi-anechoic chamber
SOLT	Short-open-load-through
STFFT	Short-time FFT
SW	Short wave
TEM	Transverse electromagnetic
TETRA	Terrestrial trunked radio
TRL	Through-reflect-line
TTE	Telephone terminal equipment
VNA	Vector network analyzer
W-CDMA	Wideband code division multiple access

Documents
Document Sharing Hub
Full document details: PD CISPR TR 16-3:2020

4 Technical reports

4.1 Correlation between measurements made with apparatus having characteristics differing from CISPR characteristics and measurements made with CISPR apparatus

4.1.1 General

CISPR standards for instrumentation and methods of measurement have been established to provide a common basis for controlling radio interference from electrical and electronic equipment in international trade.

The basis for establishing limits is that of providing a reasonably good correlation between measured values of the interference and the degradation it produces in a given communications system. The acceptable value of signal-to-noise ratio in any given communication system is a function of its parameters, including bandwidth, type of modulation, and other design factors. As a consequence, various types of measurements are used in the laboratory in research and development work in order to carry out the required investigations.

The purpose of this subclause is to analyse the dependence of the measured values on the parameters of the measuring equipment and on the waveform of the measured interference.

4.1.2 Critical interference-measuring instrument parameters

The most critical factors in determining the response of an instrument for measuring interference are the following: the bandwidth, the detector, and the type of interference being measured. Considered to be of secondary importance, but, nevertheless, quite significant in correlating instruments under particular circumstances, are: overload factor, AGC design (if used), image and other spurious responses, and meter time constant and damping.

For purposes of discussion, reference is made to three fundamental types of radio noise: impulse, random and sine wave. The dependence of the response to each of these on the bandwidth and the type of detector is given in Table 1. In Table 1, δ is the magnitude of the impulse strength, Δf_{imp} is the impulse bandwidth, Δf_{rn} is the random noise bandwidth, $P(\alpha)$ is the pulse response for the quasi-peak detector, f_{PR} is the pulse repetition frequency, and E' is the spectral amplitude of the random noise. The relative responses of various detectors to impulse interference for one instrument are shown in Figure 1.

Table 1 shows that the dependence of the noise meter response on bandwidth is different for all three types of interference. If the waveform being measured can be defined as being any of the three types listed in Table 1, and if a standard source provides that type of waveform, then by using the substitution method, a satisfactory calibration can be obtained for any instrument with adequate overload factor independent of its bandwidth. Thus, with a purely random interference or a purely impulsive interference of known repetition rate, calibration can be made using a corresponding source, or a correlation factor calculated on the basis of known circuit parameters.

If a particular interference waveform is of an intermediate type between these three types, then the correction or correlation factors will also be intermediate. In any given case, it will be necessary to classify the noise waveform in such a manner that a significant correlation factor can be established. Hence, in order to develop this subject to any significant extent, it will be necessary to examine typical interference sources and to determine the extent to which they are of impulsive, random, or sine-wave type.

If an interference measuring set with several types of detectors is available, for example, peak, quasi-peak and average, the type of interference can be assessed by measuring the ratios of the readings obtained with these detectors. These ratios will, of course, depend upon the bandwidth and other characteristics of the instrument being used for the measurement.

AVA Documents
Document Sharing Hub
Full document details: PD CISPR TR 16-3:2020

Table 1 – Comparative response of slideback peak, quasi-peak and average detectors to sine wave, periodic pulse and Gaussian waveform

Input waveform	Detector type			
	Slideback peak (sb)	Quasi-peak:1/600 (qp)	Field intensity (average)	RMS
CW sine wave	e	e	e	e
Periodic pulse (no overlap)	$1{,}41\ \delta\,\Delta f_{\text{imp}}$	$1{,}41\ \delta\,\Delta f_{\text{imp}}\ P(\alpha)$	$1{,}41\ \delta f_{\text{PR}}$	$1{,}41\ \delta\ \sqrt{f_{\text{PR}}\Delta f_{\text{imp}}}$
Random	–	$1{,}85\ \sqrt{\Delta f_{\text{rn}} E'}$	$0{,}88\ \sqrt{\Delta f_{\text{rn}} E'}$	$\sqrt{\Delta f_{\text{rn}} E'}$

Key

e is the RMS value of the applied sine wave.

$P(\alpha)$ is given in Figure 2.

E' is the spectral strength in RMS V/Hz bandwidth.

δ is the impulse strength. It is assumed the instrument is calibrated in terms of the RMS value of a sine wave. It is assumed that characteristics of the envelope are measured by the detector on random noise.

Δf_{imp} is the impulse bandwidth.

Δf_{rn} is the random noise bandwidth.

f_{PR} is the pulse repetition frequency.

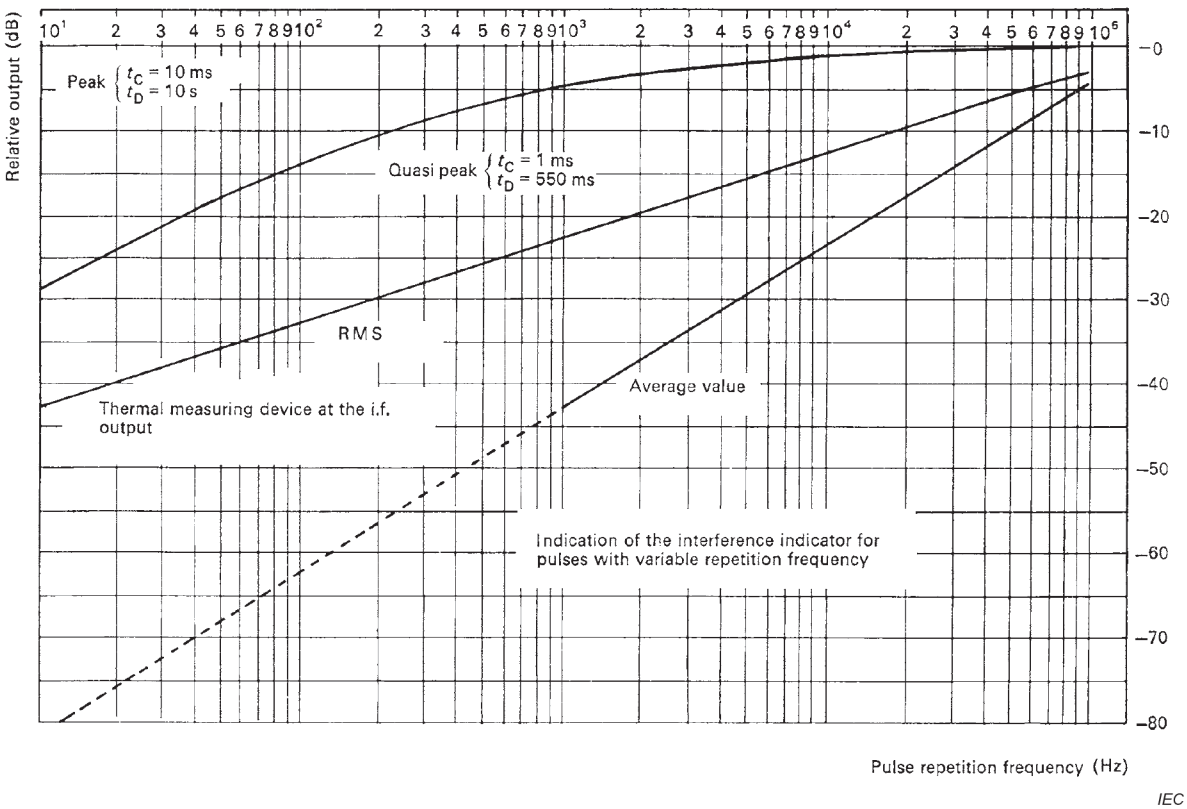

Figure 1 – Relative response of various detectors to impulse interference

Documents
Document Sharing Hub
Full document details: PD CISPR TR 16-3:2020

4.1.3 Impulse interference – correlation factors

The quasi-peak detector response of any interference measuring set to regularly repeated impulses of uniform amplitude can be determined by the use of the "pulse response curve" which is shown in Figure 2. This figure shows the response of the detector in percentage of peak response for any given bandwidth and value of charge resistance and discharge resistance. Applying this curve, it should be noted that the peak itself is dependent upon the bandwidth, so that as the bandwidth increases, the peak value increases, but the percentage of peak, which is read by the detector, decreases; over a narrow range of bandwidth, these effects tend to counteract each other. The bandwidth used in this curve is the 6 dB bandwidth, which for the passband characteristics typical of most interference measuring equipment, is about 5 % less than the so-called impulse bandwidth. A theoretical comparison of instruments having various bandwidths and detector parameters with the CISPR instrument is shown in Figure 3.

The response of the average detector to impulsive noise is an interesting case. The reading of an average detector for impulsive noise is independent of the bandwidth of the pre-detector stages. It is, of course, directly proportional to the repetition rate. In most cases, the reading obtained with an average detector for impulsive noise is so low as to be of no practical value unless the noise meter bandwidth is exceedingly narrow, such as of the order of a few hundred hertz. For a repetition rate of 100 Hz and a bandwidth of the order of 10 kHz, the average value would be approximately 1 % of the peak value. Such a value is too low to measure with any degree of precision. Furthermore, for many communication systems, the annoyance effect may be well above the reading obtained with the average meter. This, of course, is one of the justifications for the use of the quasi-peak instrument.

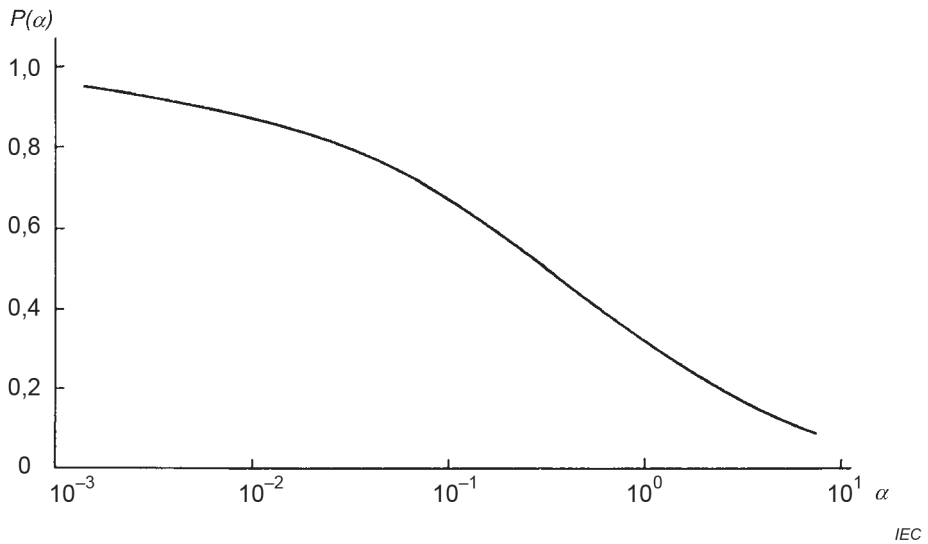

$$\alpha = \frac{(\pi R_c \Delta F)}{(R_d f_{PR})}$$

Key

R_c charging resistance, in Ω

R_d discharging resistance, in Ω

ΔF 6 dB bandwidth, in Hz

f_{PR} pulse repetition frequency, in Hz

Figure 2 – Pulse rectification coefficient $P(\alpha)$

Documents
Document Sharing Hub
Full document details: PD CISPR TR 16-3:2020

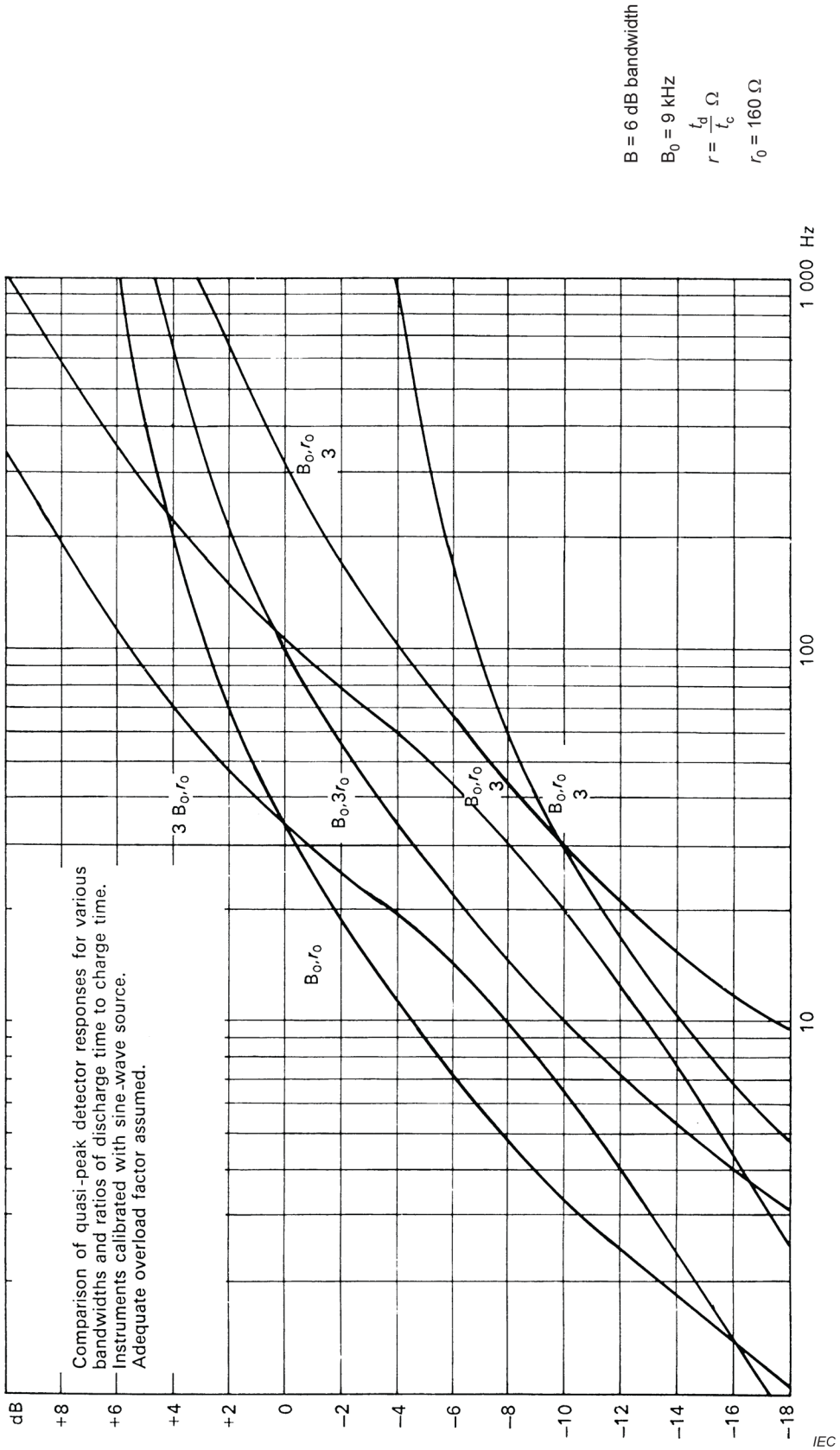

Figure 3 – Pulse repetition frequency

Documents
Document Sharing Hub
Full document details: PD CISPR TR 16-3:2020

4.1.4 Random noise

The response of a noise meter to random noise is proportional to the square root of the bandwidth. This result is independent of the type of detector used. The ratio of the random noise bandwidth to the 3-dB bandwidth is a function of the type of filter circuit. On the other hand, it has been shown that for many circuits typical of those used in interference measuring equipment, a value of about 1,04 for the ratio of effective random noise bandwidth to the 3 dB bandwidth is a reasonable figure.

4.1.5 The root mean square (RMS) detector

One of the advantages of the RMS detector in correlation work is that for broadband noise the output obtained from it will be proportional to the square root of the bandwidth, i.e. the noise power is directly proportional to the bandwidth. This feature makes the RMS detector particularly desirable and is one of the main reasons for adopting the RMS detector to measure atmospheric noise. Another advantage is that the RMS detector makes a correct addition of the noise power produced by different sources, for example, impulsive noise and random noise, thus for instance allowing a high degree of background noise.

The RMS values of noise often give a good assessment of the subjective effect of interference to AM sound and television reception. However, the very wide dynamic range needed when using very wide-band instruments for measuring impulsive noise, limits the use of RMS detectors to narrow-band instruments.

4.1.6 Discussion

The preceding paragraphs have indicated the theoretical basis for comparing measurements obtained with different instruments. As mentioned previously, the possibility of establishing significant correlation factors depends upon the extent to which noise can be classified and identified so that the proper correlation factors may be used. In many frequency ranges, impulsive interference appears to be the most serious; however, for power lines where corona interference is the primary concern, random interference would be expected to be more characteristic. Additional quantitative data are needed on typical interference characteristics. Another important parameter is the overload factor.

4.1.7 Application to typical noise sources

4.1.7.1 Commutator motors

The noise generated by commutator motors is usually a combination of impulse and random noise. The random noise originates in the varying brush contact resistance, while the impulse noise is generated from the switching action at the commutator bars. For optimum adjustment of commutation, the impulse noise can be minimized. However, where variable loading is possible, measurements have confirmed that for the peak and quasi-peak detectors, the dominant noise is of impulse type and the random component may be neglected. While the repetition rate may be of the order of 4 kHz, the effective rate is lower because the amplitude of the impulses is usually modulated at twice the line frequency. Hence, experimental results have shown that quasi-peak readings are consistent with bandwidth variations if the repetition rate of the impulse is assumed to be twice the line frequency.

Peak measurements show fluctuating levels on such noise because of the irregular nature of the commutator switching action.

The quasi-peak to average ratio is lower than would be obtained for pure impulse noise for two reasons:

1) the modulation of the commutator switching transients by line frequency produces many pulses below the measured quasi-peak level. These pulses do not contribute to the quasi-peak value but do contribute to the average.

Documents
Document Sharing Hub

Full document details: PD CISPR TR 16-3:2020

2) the relatively low level, but continuous, random noise can likewise contribute substantially only to the average value. Experimental values of quasi-peak to average ratio ranged from 13 dB to 23 dB with the highest ratios for the widest bandwidths (120 kHz).

4.1.7.2 Impulsive sources

Tests on an ignition model, commutator motor appliances, and appliances using vibrating regulators showed reasonable agreement on instruments with the same nominal bandwidth, but with time constant ratios of the order of 3:1 on restricted portions of the output indicator scale. Deviations at higher scale values are without explanation. Relatively poor correlation was obtained on sources producing very low repetition rate pulses.

4.1.7.3 Ignition interference

"CISPR Recommendation 35" recognizes that correlation between quasi-peak and peak detectors can be established as a practical matter. The conversion factor of 20 dB is explained partly on the basis of theory for uniform repeated impulses, and partly on the basis of the actual irregularity of the amplitude and wave shape of such impulses.

NOTE "CISPR Recommendation 35", from CISPR 7:1969, *Recommendations of the CISPR*, is quoted for reference:

" RECOMMENDATION No. 35
THE CORRELATION BETWEEN PEAK AND QUASI-PEAK MEASUREMENTS OF INTERFERENCE FROM IGNITION SYSTEMS
(This Recommendation closes Study Question No. 45 of 1961)
(Stockholm, 1964)

The C.I.S.P.R.,
CONSIDERING
that for the measurement of interference from the ignition systems of internal combustion engines there will, in general, be two types of detector, namely, peak and quasi-peak;

RECOMMENDS
that a correlation factor of 20 dB between peak and quasi-peak measurements of interference from ignition systems be adopted for frequencies in the range covered by C.I.S.P.R. Publication 2, i.e. when peak measurements are made the acceptable limits are 20 dB above the corresponding quasi-peak measurements; for peak measurements the engine may be operated at any speed above idling speed but for quasi-peak measurements the speed should be set as near as possible to 1 500 rev/min for multi-cylinder engines and 2 500 rev/min for single cylinder engines."

4.1.7.4 Dependence on bandwidth

Comparisons of measurements made in the UK with two instruments having bandwidths of 90 kHz and 9 kHz respectively have been reported to show that for most interference sources, the values obtained are in the ratio 14 dB to 18 dB. This figure is consistent with the concept that the interference is dominated by impulse type noise but that some random components are present.

4.1.8 Conclusions

Analysis of data comparing the responses of various instruments shows that, in almost every case, it is possible to explain the differences in measured values on the basis of theoretical and practical considerations. In many instances, it is indicated that waveform characteristics are known to predict correlation factors adequately with an accuracy of 2 dB to 4 dB.

Further studies are needed:

a) to characterize in some detail the waveforms of various sources of interference, and
b) to correlate these waveform characteristics with measured values and the instrument parameters.

Documents
Document Sharing Hub
Full document details: PD CISPR TR 16-3:2020

4.2 Interference simulators

4.2.1 General

Interference simulators can be used for various applications, in particular to study signal processing in systems and equipment in the presence of interference (for example, overloading of receivers, synchronization of TV receivers, error rate of data signals, etc.) and for assessment of the annoyance caused by disturbances in broadcast and communication services.

A simulator should produce a stable and reproducible output signal, which requirement is normally not fulfilled by an actual interference source, and the simulator output waveform should show a good resemblance to the actual interference signal.

4.2.2 Types of interference signals

The following interference sources can be simulated.

a) Narrowband interference sources generating sine-wave signals, for example receiver oscillators and ISM equipment. An appropriate RF standard signal generator can be used to simulate these sources. ISM interference is often modulated by the mains voltage, which can be simulated by modulating the RF signal with a full-wave rectified mains signal.

b) Broadband interference sources producing continuous broadband noise, for example, gaseous discharges and corona. For simulating purposes a standard broadband noise source (saturated vacuum tube diode, zener diode or gas tube followed by a suitable broadband amplifier) can be used. In mains-fed sources of this type, mains modulation is present, but because of the non-linear behaviour of gaseous discharges the envelope of the actual noise signal can deviate appreciably from the normal full-wave rectified mains waveform. In this case, gating the noise of the simulator at a repetition frequency of twice the mains frequency can yield a good correspondence with the actual interference signal.

c) Thyristor controlled regulators with phase control generate narrow pulses of constant amplitude in an RF-channel at a repetition frequency equal to twice the mains frequency. Standard pulse generators with narrow output pulses (10^{-7} s to 10^{-9} s width) of the same repetition frequency can be used to easily simulate these sources.

d) Ignition systems, mechanical contacts and commutator motors generate short periods (bursts) of quasi-impulsive noise. This type of noise is caused by very short pulses of regular or irregular height at random time intervals; if the average interval between adjacent pulses is less than the reciprocal of the channel bandwidth under test ($\tau_{av} < 1/B$), the pulses overlap, and because of the random phase conditions, a random fluctuating output signal (noise) results. Therefore, bursts of quasi-impulsive interference of this type can be simulated by a gated broadband noise signal.

The duration and the repetition frequency of the bursts depend on the type of interference source (see Table 2).

Ignition interference is characterized by burst durations between 20 μs and 200 μs and repetition frequencies between 30 bursts/s and 300 bursts/s depending on the number of cylinders and revolutions/min of the engine.

Mechanical contacts produce bursts (clicks) which can vary between some milliseconds (snap-off switches) and more than 200 ms. In the case of a contact device in a mains-fed circuit, the noise during the burst is modulated with the full-wave rectified mains voltage.

Commutator motors produce much shorter bursts with durations between 20 μs and 200 μs at repetition frequencies between 10^3 bursts/s and 10^4 bursts/s, depending on the number of commutator bars and revolutions per minute of the rotor. Also in this case, the mains supply causes a similar envelope modulation of the noise bursts.

Documents
Document Sharing Hub
Full document details: PD CISPR TR 16-3:2020

4.2.3 Circuits for simulating broadband interference

Simulators of this type should generate gated noise bursts with or without mains modulation according to the characteristics specified in Table 2. Figure 4 shows a straightforward design with a noise source followed by an appropriate amplifier of 70 dB to 80 dB gain, a gating circuit to simulate the bursts, a mains envelope modulator and an output attenuator to adjust the required output level.

Table 2 – Characteristics of gate generator and modulator to simulate various types of broadband interference

Simulator signal	Burst duration	Burst repetition frequency	Mains modulation [a]
Gaseous discharge		Continuous	Yes/no [b]
Ignition	20 µs to 200 µs	30 bursts/s to 300 bursts/s	No
Switches	5 ms to 500 ms	0,2 bursts/min to 30 bursts/min, or single	Yes/no
Commutator motors	30 µs to 300 µs	10^3 bursts/s to 10^4 bursts/s	Yes/no

[a] Depending on AC or DC supply.

[b] In the case of mains modulation, gating at a repetition frequency $2f_{mains}$ and gate width of 1 ms to 2 ms may be more appropriate.

The disadvantage of this layout is that a wide usable frequency range requires a broad bandwidth for the entire circuit between noise source and output terminal. The most critical part in this respect is the high-gain amplifier. For applications in a wide frequency range (for example, 0 MHz to 1 000 MHz) such a range can be split up in several smaller ranges or a tunable amplifier may be used. Such a design complicates the construction of the simulator appreciably.

Another way to produce a gated wideband noise signal is given in the diagram of Figure 5. In this design, nanosecond pulses are generated in the output stage, for example, a step recovery diode or similar device. These pulses of constant height are triggered at random time intervals and at a sufficiently high repetition rate to cause overlap in the RF channel under test in order to result in quasi-impulsive noise in the output of the channel. Average repetition rates of a few megahertz are required for measurements in a TV channel of at least 100 kHz for measurements in an FM channel and of at least 10 kHz in an AM channel. The random occurrence of the trigger pulses is obtained from the zero crossings of a broadband signal. For this purpose the output of a noise source is fed to an appropriate amplifier which is followed by a gating circuit for burst simulation. The gated noise signal is fed to a bistable multivibrator which converts the zero crossings into pulses of random varying width from which narrow trigger pulses at random distances are generated by the monostable multivibrator.

The advantage of this system over the circuit of Figure 4 is that the usable frequency range is determined by the output pulses of the step-recovery diode only. An example of such a circuit is given in Figure 6, in which circuit output pulses are generated by the step recovery diode HP0102, the pulse width is determined by the length of a short-circuited coaxial cable L. Ringing effects are suppressed by the fast switch diode HP2301, and mains modulation can be effected simply by modulating the supply voltage of the step recovery diode with a full-wave rectified mains voltage. Pulses of 1 ns duration and 5 V amplitude are generated and offer an output spectrum flat to about 500 MHz. Such a single pulse causes a 50 mV pulse in a TV channel and a 1 mV pulse in an FM channel; overlapping pulses add up, and the peak and quasi-peak value of the resulting signal is considerably higher.

AVA Documents
Document Sharing Hub

Full document details: PD CISPR TR 16-3:2020

The bandwidth of the preceding stages which generate the trigger signal (noise source, amplifier and gating circuit) should be sufficient for the required pulse repetition rate, so for measurements in a TV channel a bandwidth of 5 MHz to 10 MHz is quite satisfactory. Moreover, the linearity of these stages is not critical because only the position of the zero crossings is important. The multivibrators have to generate steep pulses of short duration (about 0,1 μs) to drive the step-recovery diode.

In summary, the circuit according to Figure 4 is very useful for broadband interference simulators to be operated in a limited frequency range, whereas the circuit of Figure 5 is more suitable for simulators intended for wideband use.

Documents
Document Sharing Hub

Full document details: PD CISPR TR 16-3:2020

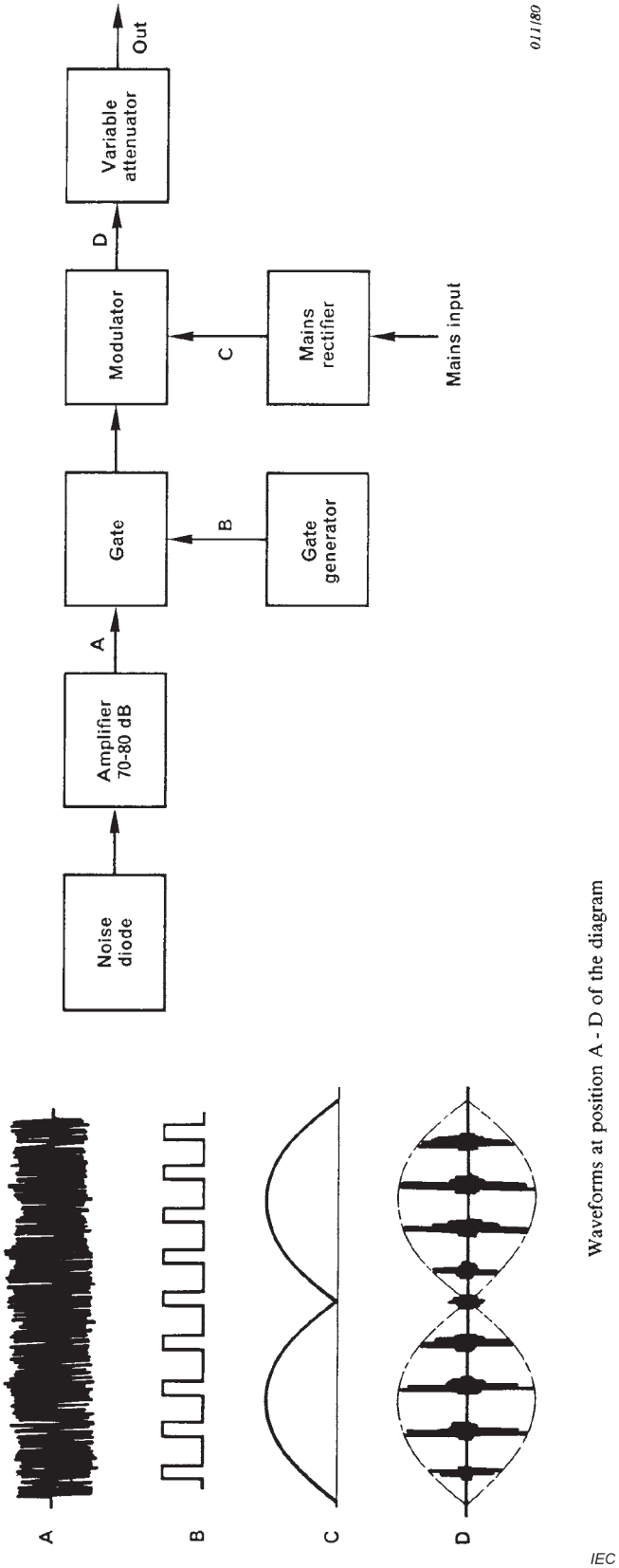

Figure 4 – Block diagram and waveforms of a simulator generating noise bursts

Documents
Document Sharing Hub
Full document details: PD CISPR TR 16-3:2020

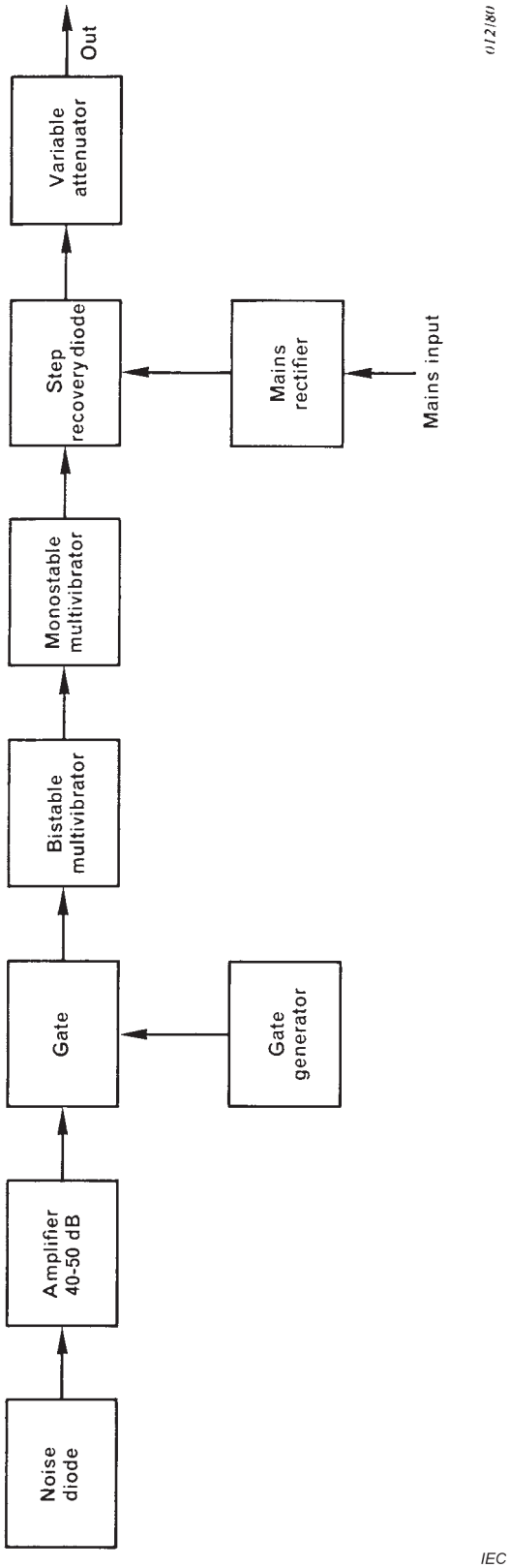

Figure 5 – Block diagram of a simulator generating noise bursts according to the pulse principle

Documents
Document Sharing Hub
Full document details: PD CISPR TR 16-3:2020

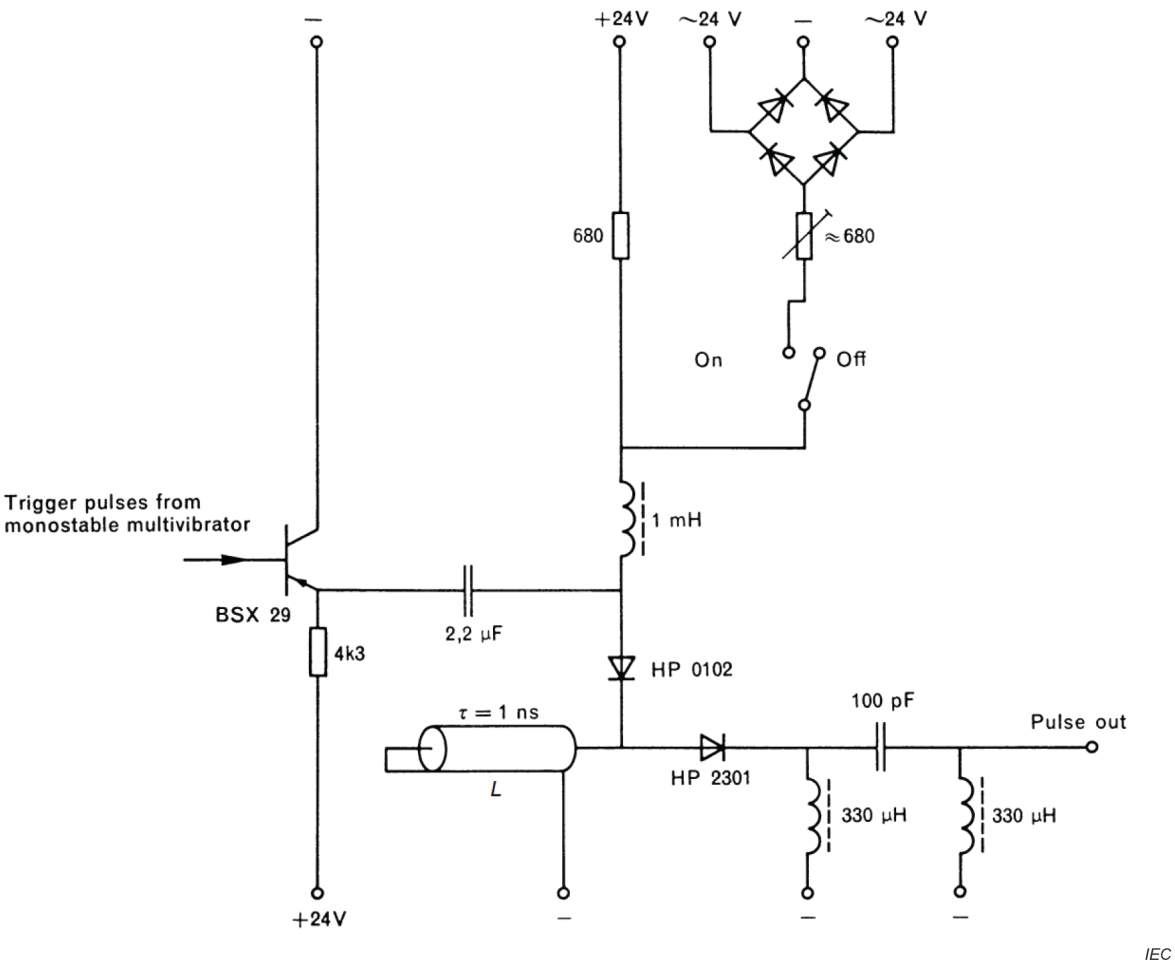

Figure 6 – Details of a typical output stage

4.3 Relationship between limits for open-area test site and the reverberation chamber

4.3.1 General

At present there are limits for use with the open-area test site method of measurement specified in several CISPR publications. For equipment that can be measured using the reverberation chamber method, a procedure is required to relate the limit to be used with that of the open-area test site (OATS) limit. The procedure is described in this subclause.

4.3.2 Correlation between measurement results of the reverberation chamber and OATS

The OATS measurement sets out to find the maximum level of radiation of an EUT (equipment under test). Whether the measurement is of the field strength or of power density at the measurement antenna, or of the power into an antenna in substitution of an EUT, the measured results can be expressed in terms of the equivalent radiated power from a half-wave dipole. Let this equivalent radiated power be P_q in dB(pW).

The reverberation chamber measures the total radiated power of the EUT. Let the measured power be P_t in dB(pW).

The two measurements are related to each other by the gain of the EUT as a radiator with respect to an isotropic radiator. Let this EUT gain be G in dB. The relationship is given by Equation (6). The equation is derived in Annex A.

Documents
Document Sharing Hub
Full document details: PD CISPR TR 16-3:2020

$$P_t + G = P_q + 2 \quad (6)$$

4.3.3 Limits for use with the reverberation chamber method

Consider the case of an EUT which is exactly on the limit, L_o, when measured in the open area test site, i.e. $P_q = L_o$.

This EUT should also be exactly on the corresponding limit, L_r, when it is measured in the reverberating chamber, i.e. $P_t = L_r$.

From Equation (6), we can relate the two limits as in Equation (7).

$$L_r = L_o + 2 - G \quad (7)$$

The value of L_r is dependent not only on L_o, but also on G. Because G will not be the same for all EUTs, it is not possible to set L_r to treat all EUTs in a manner identical to the effect of L_o. If say $L_r = L_o$, then it is correct only for EUTs with $G = 2$. EUTs with a G greater than 2 will find it easier to pass the reverberation chamber limit, and vice versa.

It is necessary to determine the value of G. This can be done from measurements of P_q and P_t. Figure A.1 shows the curves of P_q versus P_t for various values of G. The shaded region is for negative values of G. (Experimental points appearing in this region are caused by failure to locate the maximum open-site radiation, probably due to the maximum radiation lying outside of the horizontal plane).

An example is given in Figure A.2. A number of microwave ovens were measured for P_q and P_t. It can be seen that:

– for points lying in the positive G region, the majority have values around 2;
– more points lying in the positive G region as the frequency goes up, indicating that the radiation pattern is becoming more directional in the vertical direction.

Based on this evidence, the reverberation chamber results can be related to those of an OATS. In fact, use of a reverberation chamber appears to be a more effective method in the ability to measure a quantity representative of the maximum radiation.

4.3.4 Procedure for the determination of the reverberation chamber limit

The procedure to determine the reverberation chamber limit is as follows.

i) Measure a sample of equipment for the maximum radiation on an OATS. Convert the measured quantities to the equivalent power from a half-wave dipole. Call this quantity P_q, in dB(pW).
ii) Measure the same sample in the reverberating chamber for total radiated power. Call this quantity P_t, in dB(pW).
iii) The relationship between the reverberation chamber limit and the OATS limit can be found by the graphical method of Figure A.1, or by calculating the gain of each equipment, obtaining a representative value of G for the equivalent type using statistical methods, and applying Equation (7).

Documents
Document Sharing Hub
Full document details: PD CISPR TR 16-3:2020

4.4 Characterization and classification of the asymmetrical disturbance source induced in telephone subscriber lines by AM broadcasting transmitters in the LW, MW and SW bands

4.4.1 General

The use of semiconductor devices in telephone terminal equipment (TTE) has created the need to verify the immunity to RF fields of this equipment, as non-linear semiconductor devices demodulate the induced RF signals [1], [17], [18], [19], [20].[2] The latter effect gives rise to a DC shift which may alter the operating point of such a device, thus, for example, reducing the noise margin of digital devices. In the case of amplitude-modulated RF fields, the non-linearity gives rise to a baseband signal that may become audible in the telephony system. AM broadcasting transmitters in the LW, MW and SW bands form an important class of RF-field sources.

Because of the relatively small dimensions of TTE (compared to the wavelength of the disturbance signal) the asymmetrical (common-mode) source induced in telecommunication lines is expected to be the dominant disturbance source. Therefore, a conducted-immunity test (current-injection test) is relevant for this equipment. In this test, the disturbance signal is applied via the telecommunication lines. As a consequence, this subclause deals with the characterization of the unwanted antenna properties of telecommunication lines and with prediction models supplying information about the probability that certain parameter values will be met in practice. Moreover, it discusses the parameters that are of relevance when specifying the disturbance source used in the immunity test. The various considerations will be limited to parameters relevant at the subscriber end of the telephone lines.

In 4.4.2 the antenna properties will be expressed in terms of an antenna factor of the subscriber lines i.e. the induced asymmetrical open-circuit voltage normalized to the RF field strength, and an equivalent resistance of the induced asymmetrical source. The prediction models are needed in the classification of the RF fields and the induced asymmetrical disturbances, i.e. 4.4.3, and when setting immunity limits, i.e. 4.4.4. This subclause takes the view that the disturbance source in the immunity test is to be specified by an open-circuit voltage and a source impedance.

All mathematical relations associated with the derivation of the models and those needed by the user of this subclause when applying the models to the respective geographical area are given in Annex B, Annex C, Annex D, and Annex E.

This subclause is based on results of experimental investigations carried out on buried telephone-subscriber lines in Germany [21], [22] and in the Netherlands [23]. In these investigations induced-voltage and current data and magnetic-field-strength data were recorded at a large number of locations, permitting a statistical evaluation of the parameter values. A statistical approach was needed, because the telephone lines have random routing in the buildings and, consequently, random orientation with respect to the RF field makes for random coupling with nearby metal objects, while the buildings cause a random scattering of the RF fields.

It is to be expected that the contents of this subclause will also be applicable to other types of lines running through buildings in a similar manner to telephone-subscriber lines, for example, bus-system lines and signal and control lines.

4.4.2 Experimental characterization

4.4.2.1 General

A full description of the experimental characterization is presented in [22] and [23]. Therefore, this subclause contains only a summary of this method with regard to the parameters needed.

---

2 Numbers in square brackets refer to the bibliography.

Documents
Document Sharing Hub

Full document details: PD CISPR TR 16-3:2020

The induced asymmetrical voltage was measured at the outlet of a telephone-subscriber line using a modified T-network [24] and [25]. As a result of this modification, a voltage U_h could be measured across a 10 kΩ resistor and a voltage U_l across a 150 Ω resistor. The investigations showed that U_h could be considered as the induced open-circuit voltage. In practice, the reference for this voltage is generally unknown. During the measurements that reference was a special metal measuring cart connected via a copper strap to the central heating system. The equivalent resistance R_a of the induced source is estimated from data pairs $\{U_h, U_l\}$.

At each location two magnetic-field-strength data of the broadcasting transmitter were measured using a loop antenna positioned in a vertical plane and rotated about its vertical axis to find the maximum reading. One datum, H_i, was measured near the outlet under investigation inside the building, and one datum, H_o, was measured outside the building at a distance of about 10 m from that building. In order to obtain a sufficiently high induced-signal-to-ambient-noise ratio, the measurements were carried out in areas with a relatively high value of the RF field strength. This is not expected to influence the applicability of the results, as the presence of a broadcasting transmitter is not taken into account in the layout of telephone-subscriber lines. Moreover, as mentioned in 4.4.1, the induced voltage will be normalized to the field strength and the resulting "antenna factor" will represent a property of the subscriber lines measured.

4.4.2.2 Field strength and building effect

Although the RF field is not a characteristic of the subscriber lines, it forms the origin of the induced disturbances. Two aspects of the RF field will be considered in this subclause:

a) The measured field strength H_o outside the buildings compared to the field strength H_c calculated from the simple far-field relation for a half-wave dipole (in its main direction):

$$H_c = \frac{7\sqrt{P}}{Z_0 r} \tag{8}$$

where

P is the transmitter power;

Z_0 is free-space wave impedance (377 Ω) and

r the distance between the transmitter and the point of observation.

In the calculations, the values of P as given in [28] are used.

NOTE Although broadcast transmitter antennas usually are monopoles (in the frequencies of interest), the half-wave dipole formula in Equation (8) has been used for convenience.

b) The effect of the building on the field strength, which can be expressed in a building-effect parameter A_b defined by:

$$A_b = H_o - H_i \tag{9}$$

where H_o and H_i are in dB(μA/m).

This factor is often called the building attenuation. However, this factor not only depends on the attenuation properties of the building material itself, but also on the re-radiation properties of metallic structures in and near the building, and on the height above ground at which H_o and H_i were measured. Therefore the term building effect is used in this subclause.

A consideration of these two aspects is needed in view of the antenna factors to be discussed in 4.4.2.3 and in view of the prediction models to be discussed in 4.4.2.4.

Documents
Document Sharing Hub
Full document details: PD CISPR TR 16-3:2020

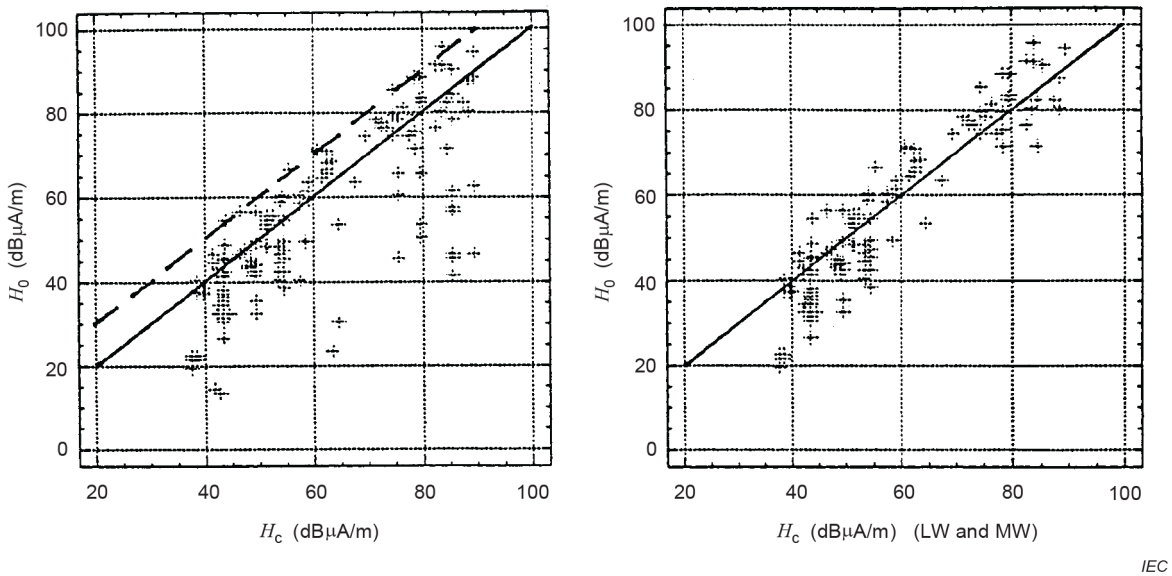

a) All data **b) Data of SW transmitters rejected**

Figure 7 – Scatter plot of the measured outdoor magnetic field strength H_o (dBμA/m) versus the calculated outdoor magnetic field strength H_c dB(μA/m)

The results of $H_o(H_c)$ given in Figure 7a) show that large deviations from $H_o = H_c$ are possible (solid line), but that $H_o \leq (H_c + 10)$ dB(μA/m) (dashed line), hence the measured value is at most a factor of 3 higher than the value calculated from Equation (8). The largest deviations concern data of SW transmitters. This is understandable, because SW transmitters normally have a beamed antenna pattern, whereas the antenna patterns of the LW and MW transmitters are generally close to circular. Figure 7b) gives the scatter plot $H_o(H_c)$ after rejection of the SW transmitter data.

Documents
Document Sharing Hub
Full document details: PD CISPR TR 16-3:2020

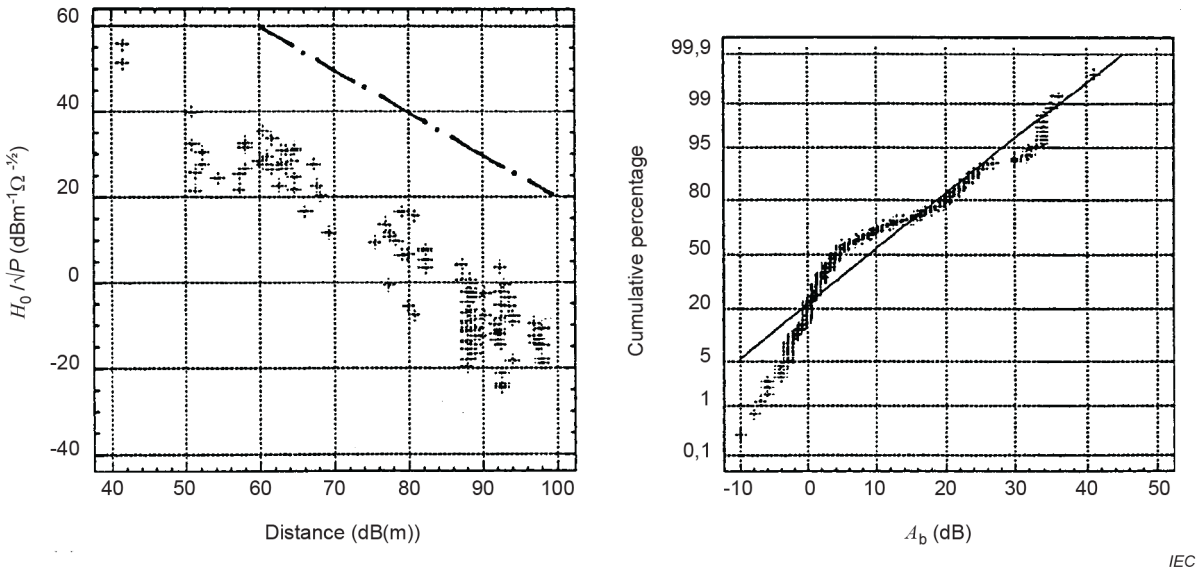

a) Scatter plot of the measured outdoor magnetic field strength H_o normalized to the square root of the reported power [26] versus the distance d (m) to the transmitter

b) Normal probability plot of the building-effect parameter A_b dB, all data

Figure 8 – Measured outdoor magnetic versus distance, and probability of the building-effect parameter

Figure 8a) shows the ratio $H_o/\sqrt{P}$ versus the distance between the point of observation and the transmitter, and the dash-dot line indicates a slope –1. It can be concluded that, on average, the data follow this slope fairly well. The associated intercept is higher than that expected from Equation (8), which is in agreement with the (H_c + 10) dBμA/m limit observed in Figure 7.

Figure 8b) shows the normal probability plot of all building-effect data. If these data were normally distributed, a straight line would have resulted. This is not the case, and the data suggest that, in a first-order approximation, two distributions are superimposed. The two distributions are found when distinguishing between data associated with buildings constructed from brick and/or wood (B/W) and data associated with buildings constructed from reinforced concrete (C). The normal probability plots of these distributions are given in Figure 9a) and Figure 9b). The negative values of A_b predominantly stem from measurements where H_i was measured on an upper floor of the building, whereas H_o was already measured at about 1,5 m above ground level outside the building. Effects of re-radiation also influence the actual field-strength data.

Documents
Document Sharing Hub
Full document details: PD CISPR TR 16-3:2020

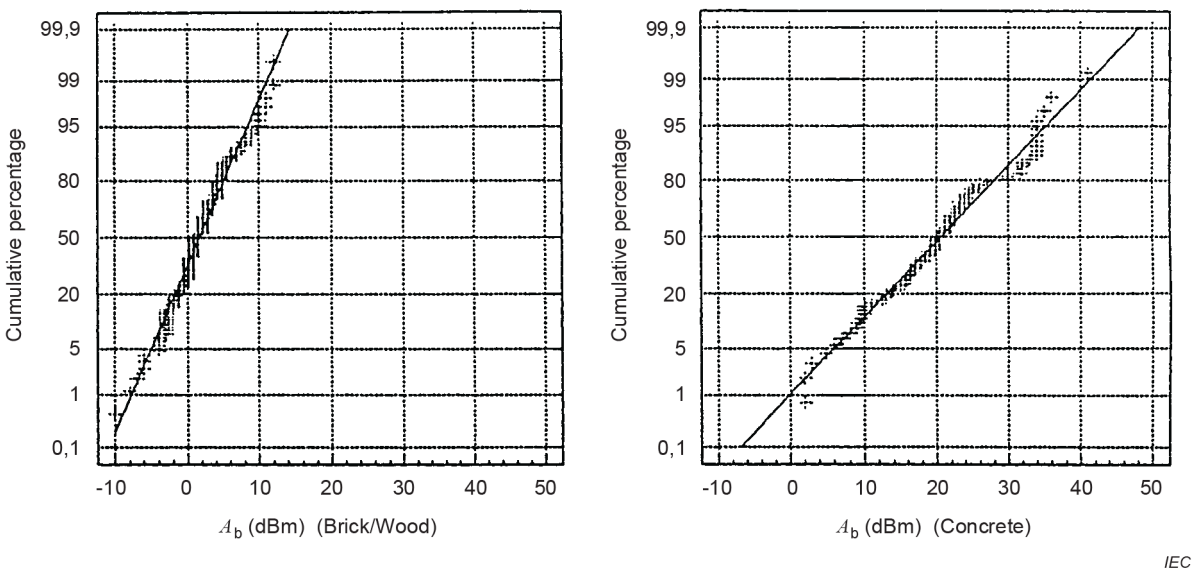

a) Buildings constructed from brick and/or wood **b) Buildings constructed from reinforced concrete**

Figure 9 – Normal probability plot of the building-effect parameter A_b dB

The numerical results have been summarized in Table 3. No clear frequency dependence of the A_b data could be observed (see 4.4.2.5).

Table 3 – Summary results of building-effect, A_b, analysis

Building material	Average dB	Standard deviation dB	Median dB	Number of data
Brick and/or wood	1,6	4,0	1,0	138
Reinforced concrete	20,6	8,7	20,1	84

4.4.2.3 The asymmetrical open-circuit voltage normalized to the field strength

4.4.2.3.1 General

The interface for the voltage measurements was the outlet to which the telephone set was connected during the measurements. The investigations showed that the influence on the measured voltages of the telephone set and its standard lead (4 m long) could be neglected.

The measured voltage will be normalized to the measured magnetic field strength in 4.4.2.3.2, and assuming far-field conditions, to the electric field strength in 4.4.2.3.3. After that, 4.4.2.3.4 deals with truncation of the distributions found in 4.4.2.3.2 and 4.4.2.3.3.

Documents
Document Sharing Hub
Full document details: PD CISPR TR 16-3:2020

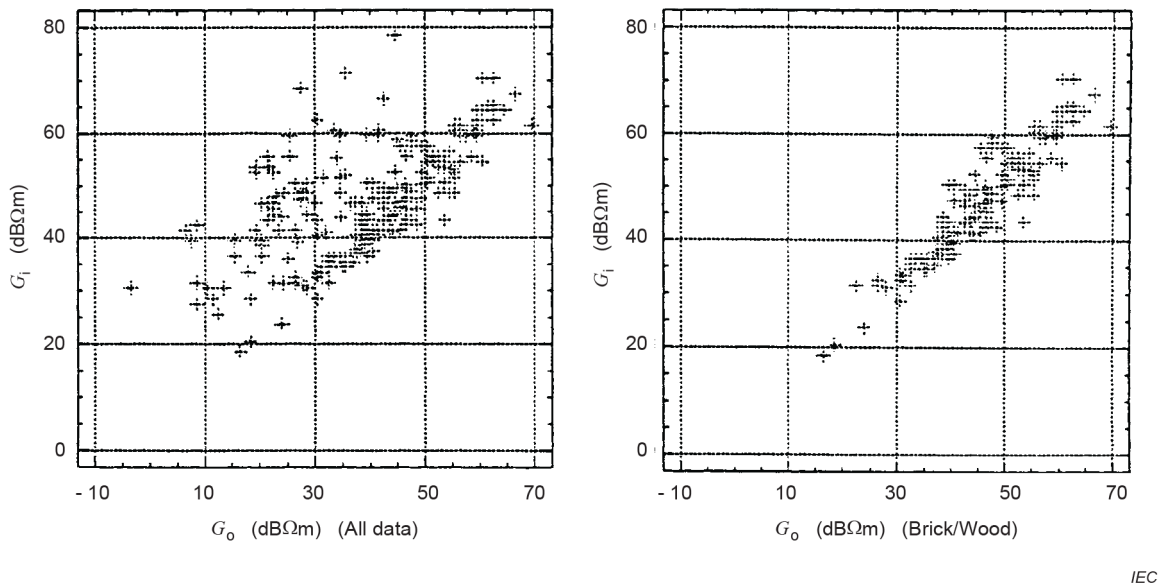

a) All data

b) Data associated with buildings constructed from brick and/or wood

Figure 10 – Scatter plot of the outdoor antenna factor G_o dB(Ωm) versus the indoor antenna factor G_i

4.4.2.3.2 *G* factors

To obtain an antenna property of the subscriber lines, the open-circuit voltage U_h is normalized to the field strength (H_i or H_o), yielding the antenna factors G_i and G_o defined by

$$G_{i,o} = \frac{U_h}{H_{ino}} \tag{10}$$

where

$G_{i,o}$ is in Ωm,

U_h is in μV, and

H_{ino} is in μA/m.

Figure 10a) shows the scatter plot $G_i(G_o)$ using all data. The plot suggests that there is one dominant "cloud" of data with a limited scattering and a second "cloud" with much more scattering. Further investigation revealed that the first cloud stems from data measured in buildings constructed from brick and/or wood, see Figure 10b), while the other cloud is associated with buildings constructed (predominantly) from reinforced concrete. Consequently, the building effect discussed in 4.4.2.2 is of importance.

Documents
Document Sharing Hub
Full document details: PD CISPR TR 16-3:2020

The normal probability plots of G_i dB(Ωm) and G_o dB(Ωm) associated with the two types of building material considered, are given in Figure 11. It can be concluded that the data follow a normal distribution, which means lognormal distributions of the G factors in Ωm. The numerical results have been summarized in Table 4, where G_U and G_L are the upper and lower limit of the range of experimental G data (see 4.4.2.3.4). The differences between G_i and G_o of the two classes of building material considered are consistent with the building-effect data for these buildings (see Table 3). No clear frequency dependence could be observed (see 4.4.2.5).

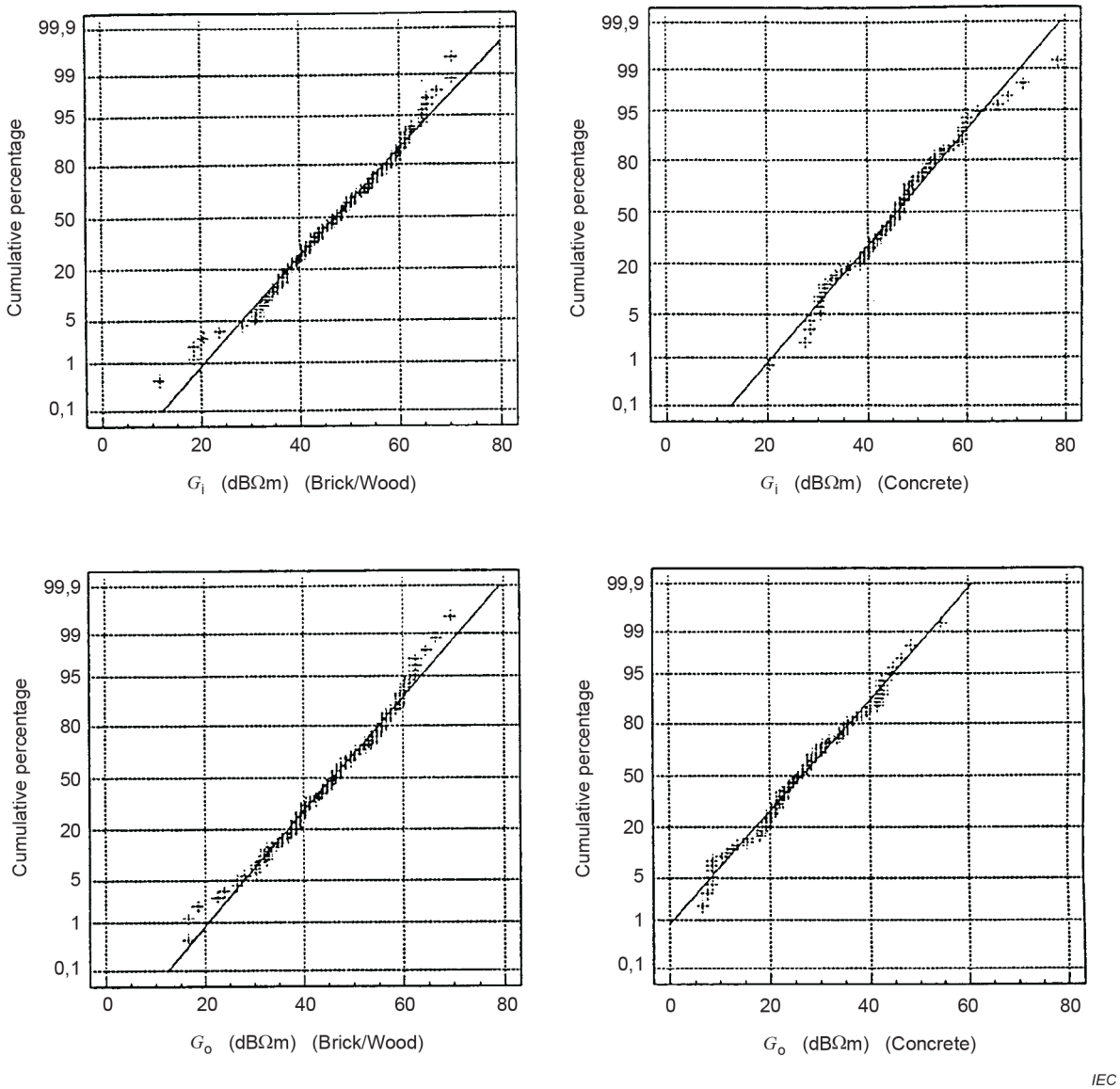

a) G_i dB(Ωm) and c) G_o dB(Ωm), associated with buildings constructed from brick and/or wood

b) G_i dB(Ωm) and d) G_o dB(Ωm), associated with buildings constructed from reinforced concrete

Figure 11 – Normal probability plots of the antenna factors

Documents
Document Sharing Hub
Full document details: PD CISPR TR 16-3:2020

Table 4 – Summary of results of G-factor analysis

G factor	Building material	Average dB(Ωm)	Standard deviation dB	Median dB(Ωm)	Number of data points
G_i	B/W	47,3	11,2	47,5	135
G_i	C	45,9	10,5	46,5	88
G_o	B/W	45,8	10,6	46,4	134
G_o	C	26,5	10,9	26,0	90

4.4.2.3.3 L factors

In 4.4.2.3.2, U_h was normalized to the measured magnetic field strength, thus yielding the G factors. Assuming far-field conditions, the electric field strength follows from E = Hz_0 with Z_0 = 377 Ω. If the outdoor field strength is considered, this assumption seems to be reasonable and the G_o factor can be converted into an L_o factor defined by

$$L_o = \frac{G_o}{Z_0} = \frac{U_h}{H_o Z_0} = \frac{U_h}{E_o} \tag{11}$$

where U_h is in μV and E_o is in μV/m.

The L factor can be considered as the effective length or effective height of the subscriber line acting as an antenna. The results for L_o have been summarized in Table 5, where L_U and L_L are the upper and lower limit of the range of experimental L factors (see 4.4.2.3.4).

Table 5 – Summary of L_o factors (far-field)

L factor	Building material	Average[a] dB(m)	Standard deviation dB	L_U dB(m)	L_L dB(m)
L_o	B/W	–5,7	10,6	18,0	–35,0
L_o	C	–25,0	10,9	3,0	–55,0
[a] Note that dB(m) refers to dB with respect to 1 m.					

In the literature an L factor of –3,0 dB(m) average (standard deviation 10 dB, number of data points = 10) has been reported [27] for a cable running 1 300 m underground and 1 000 m to 3 000 m overhead (aerial cable) towards the subscriber. Broadcasting frequencies were 594 kHz and 1 242 kHz. No details were given about the field-strength measurements, the reference for the asymmetrical voltage and the properties of the building material. The results reported in [27] are in line with the results for L_o (B/W), as given in Table 5. However, more recent investigations by the same team [29] indicate an average L-factor of 0 dB(m).

L_i factors might be derived from the G_i factors in a similar way as the L_o factors. However, it is to be expected that inside the buildings the far-field conditions are not satisfied and it has to be decided which wave impedance has to be taken. Therefore, no L_i data have been presented in Table 5. See also NOTE 2 at the end of 4.4.4.2.

4.4.2.3.4 Truncation

In 4.4.2.3.2 it was concluded that the distribution $f(G)$ of the G factors (antenna factors) is lognormal or in mathematical form

Documents
Document Sharing Hub
Full document details: PD CISPR TR 16-3:2020

$$f(g)dG = \frac{1}{G\sigma\sqrt{2\pi}} \mathrm{e}^{(\ln G-\mu)/2\sigma^2}\, dG \tag{12}$$

However, by adopting this lognormal distribution it is automatically assumed that a G factor may range from zero to infinitely large. In practice, infinitely large will never occur as wavelength effects and effects of coupling with nearby structures create an upper limit (G_U or L_U) of the antenna factors [28]. Consequently, for correct use in the prediction models (4.4.3 and 4.4.4) $f(G)$ has to be truncated. Similarly, truncation has to be applied to the distribution of the building-effect parameters.

Unfortunately, no theoretical study is known which predicts the upper limit of G (or L) of an actual telephone-subscriber line taking into account the length and the routing of a line inside the building and, buried, outside the building. However, it has to be expected that such a limit exists and the best approach is to use the experimental upper limit (G_U or L_U).

In addition to the upper limit, one may also consider a lower limit (G_L or L_L) and truncate $f(G)$ at the lower end. It is found that in the range of parameter values to be considered in 4.4.3 and 4.4.4, the influence of G_L (or L_L) is negligible.

The truncated probability density function reads

$$f_t(G)dG = \frac{f(G)dG}{\int_{G_L}^{G_U} f(G)dG} = \frac{f(G)dG}{F(G_U) - F(G_L)} = \alpha_t f(G)dG \tag{13}$$

The mathematical form of the cumulative distributions $F(G_U)$ and $F(G_L)$ is given in Annex E. Table 6 summarizes the truncation data of the G factors and the building-effect parameter A_b. Note that αt differs very little from 1, that is from the value of αt if $-\infty \leq G$ dB(Ωm) $\leq \infty$ or $-\infty \leq A_b$ (dB) $\leq \infty$ because $F(\infty) = 0{,}5$ and $F(-\infty) = -0{,}5$. The upper and lower limit in dB(m) of the L factor range are found by subtracting 51,5 dB(Ω) from the corresponding G factors in dB(Ωm).

Table 6 – Summary of truncation parameters of $f(G)$

G factor or A_b	Building material	G_U dB(Ωm) A_{bu} (dB)	G_L dB(Ωm) A_{bl} (dB)	$F(G_U)$ $F(A_{bu})$	$F(G_L)$ $F(A_{bl})$	αt_G αt_A
G_i	B/W	70,5	11,5	0,480 5	–0,499 3	1,021
G_i	C	78,5	20,5	0,498 5	–0,492 2	1,009
G_o	B/W	69,5	16,5	0,487 3	–0,497 1	1,016
G_o	C	54,5	–3,5	0,495 0	–0,497 1	1,008
A_b	B/W	12,0	–10,0	0,495 3	–0,498 1	1,007
A_b	C	41,0	2,0	0,490 5	–0,483 7	1,026

4.4.2.4 The equivalent asymmetrical-source resistance

The equivalent resistance of the induced asymmetrical source can be determined from data pairs $\{U_h, U_l\}$, where U_h is the open-circuit voltage and U_l the voltage measured across 150 Ω, using the simple relation:

Documents
Document Sharing Hub
Full document details: PD CISPR TR 16-3:2020

$$R_a = \frac{U_h - U_l}{U_l} 150\ (\Omega) \tag{14}$$

The normal probability plot of R_a dB(Ω) is given in Figure 12. It can be concluded that R_a in dB(Ω) follows a normal distribution and, hence, R_a in Ω follows a lognormal distribution. The numerical results have been summarized in Table 7. The average value found is close to the value 150 Ω used in existing immunity tests [24], [14]. In Table 7, R_{au} and R_{al} are the upper and lower limit of the range of experimental R_a data. The relatively large and small values of R_{au} and R_{al} compared to the average value of R_a stem from resonances and anti-resonances in the common mode circuit of the subscriber line. No clear frequency dependence of R_a could be observed (see 4.4.2.5), and no influence of the building material was observed.

Table 7 – Summary results of equivalent-resistance analysis

R_a (average) dB(Ω)	Standard deviation dB	Median dB(Ω)	R_a (average) Ω	Number of data points	R_{au} dB(Ω)	R_{al} dB(Ω)	R_{au} Ω	R_{al} Ω
44,2	6,8	43,5	162	204	63,7	25,2	1 531	18

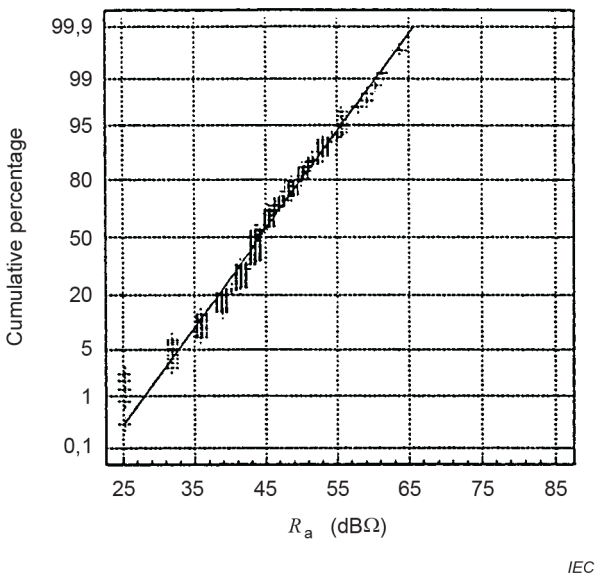

Figure 12 – Normal probability plot of the equivalent asymmetrical resistance R_a dB(Ω)

4.4.2.5 Frequency dependence of the parameters

In the frequency range determined by the measurements in the LW, MW and SW bands, no clear frequency dependence of the building effect A_b, the G factors G_o and G_i, and the equivalent resistance R_a could be observed. This is illustrated in Figure 13a) and Figure 13b) the A_b data for brick/wood buildings, the R_a data, the G_o data for brick/wood buildings, and for reinforced concrete buildings.

Documents
Document Sharing Hub
Full document details: PD CISPR TR 16-3:2020

Because no clear frequency dependence of the various quantities could be observed, it will be assumed in 4.4.3 and 4.4.4 that the building effect, the G and the L factors and the equivalent resistance are independent of the frequency in the frequency range of the LW, MW and SW bands. A possible frequency dependence is then incorporated in the standard deviation of the respective distributions.

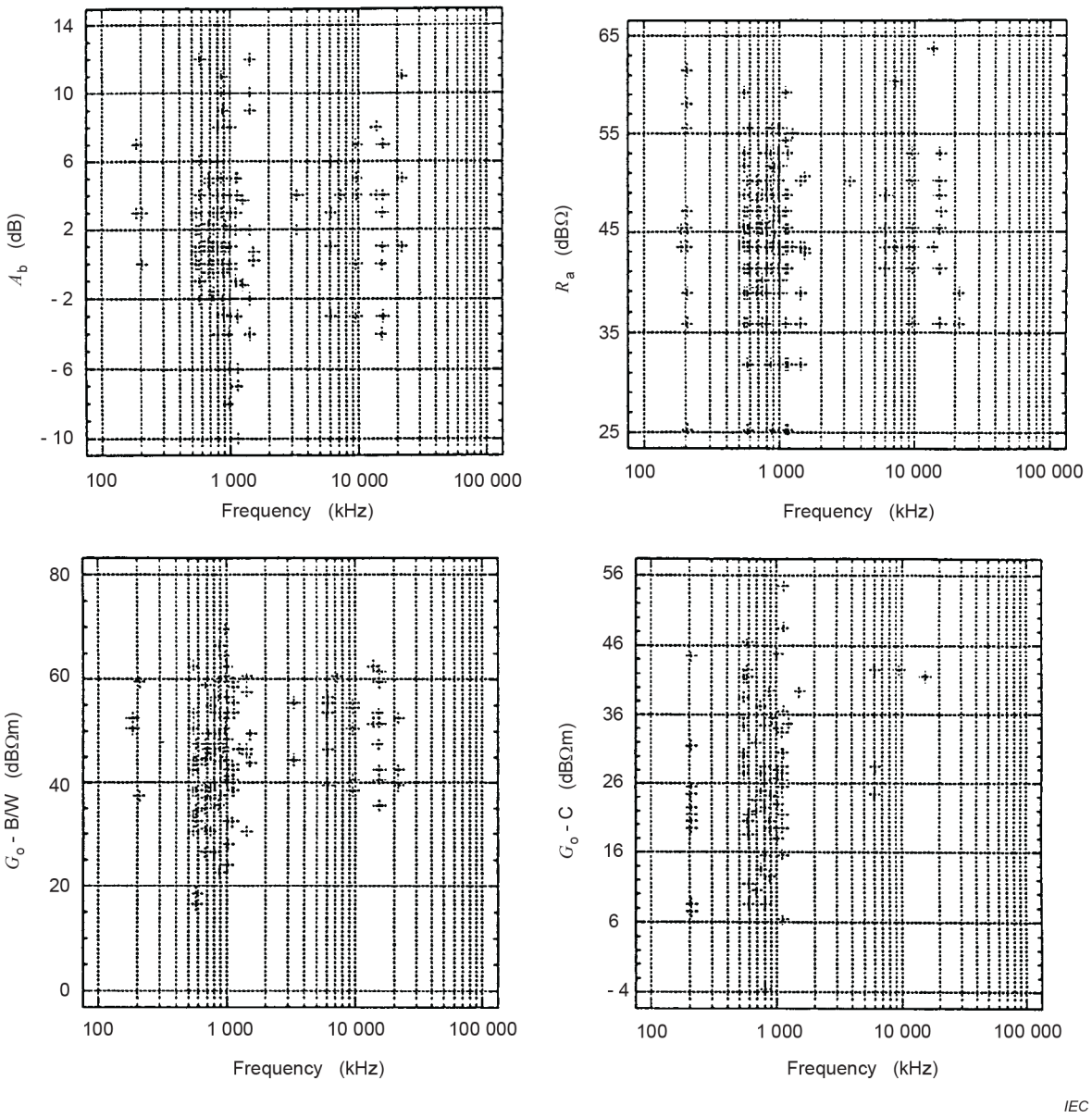

a) Building effect A_b in the case of brick/wood buildings

b) Equivalent resistance R_a

c) G_o factor for brick/wood buildings

d) G_o factor for reinforced concrete buildings

Figure 13 – Examples of the frequency dependence of some parameters

4.4.3 Prediction models and classification

4.4.3.1 General

This subclause presents some simple prediction models for fields and voltages needed in the process of classification of the electromagnetic environment and when setting immunity limits for the telephone sets to be connected to the subscriber lines.

AVA Documents Document Sharing Hub

Because the measuring locations were not chosen randomly in order to obtain a sufficiently high induced signal-to-ambient noise ratio, the basic data from which the parameters reported in 4.4.2 were derived cannot be used directly because they form a non-random sample from their actual distributions. The models to be discussed permit an estimate to be made of the complete distributions of the field strength and induced voltage. In addition, the complete distributions allow for a classification of these quantities. This subclause gives only the procedure for this classification. The actual class limits are outside its scope.

4.4.3.2 Field-strength classification

As mentioned in 4.4.2.2, the field strength is not a property of the subscriber line. Nevertheless, information about the field strength is needed in order to make a prediction of the induced voltages.

From the results given in 4.4.2.2, it follows that in a first-order approximation the outdoor field strength, to be indicated by E_o and H_o for the electric and magnetic field component respectively, is inversely proportional to the distance r between the point of observation and the transmitter, and proportional to the square root of the transmitter power. From the results summarized in 4.4.2.2 it follows that, in the worst case, the constant of proportionality is a factor of 3 (≡ 10 dB) larger than the constant of proportionality in the case of a half-wave dipole.

A classification of the outdoor electric or magnetic field strength may be based on the probability $pr\{E_o \geq E_L\}$ or $pr\{H_o \geq H_L\}$ that the outdoor field strength is greater than or equal to a given limit value, indicated by the subscript L. As explained in Annex B, this probability can be written as

$$pr\{H_o \geq H_L\} = \int_{R_L}^{H_{max}} f_n(H)dH \quad \text{or} \quad pr\{E_o \geq E_L\} = \int_{E_L}^{E_{max}} f_n(E)dH \tag{15}$$

where

$f(H)$ and $f(E)$ are the normalized field-strength distribution, and

H_{max} and E_{max} are the maximum field strength in the geographical region in which the probability has to be estimated.

Under far-field conditions both relations in Equation (15) are equivalent.

Considering a ring-shaped area (RSA) around a transmitter having a circular antenna pattern, it follows (see Annex B) that

$$pr\{E_o \geq E_L\} = \frac{\left(E_{max}^2 - E_L^2\right)E_{min}^2}{\left(E_{max}^2 - E_{min}^2\right)E_L^2} \approx \frac{E_{min}^2}{E_L^2} \tag{16}$$

where

E_{max} is the field strength at the inner boundary of the RSA, and

E_{min} is the field strength at the outer boundary of the RSA.

A similar expression is valid for the magnetic field strength (see Annex B).

Documents
Document Sharing Hub
Full document details: PD CISPR TR 16-3:2020

The inner boundary of the RSA has to be specified, as the relation between E_o and r derived from the measuring data will not be valid arbitrarily close to the transmitter, i.e. in the near-field region of the transmitter. A non-zero outer boundary field strength is needed, as E_{min} = 0 would mean that $pr\{E_o \geq E_L\}$ = 0 for all values of E_L. Note that by definition $pr\{E_o \geq E_L\}$ = 0 and that $pr\{E_o \geq E_{min}\}$ = 1 (= 100 %). The approximation given in Equation (16) is valid if $E_{max} >> \{E_{min}, E_L\}$, which is normally the case. Hence, it can be concluded that in the present model the value of E_{min} to be specified is very important. The choice of E_{min} and E_{max} will be discussed further in 4.4.4.

As an example, Table 8 gives the values of E_L for a number of probability values, assuming E_{max} = 60 V/m, which is an example of a radiation-hazard limit in the MW band of frequencies, and E_{min} = 0,01 V/m [= 80 dB(μV/m)]. The latter value is of the order of magnitude of the minimum field strength in the service area of a broadcasting transmitter. Note that the probability values are almost completely determined by E_{min}.

Table 8 – Example of field-strength classification

$pr\{E_o \geq E_L\}$	E_L	$\frac{E_{min}}{\sqrt{pr\{E_o \geq E_L\}}}$	P = 500 kW	
			k = 7 R_L	k = 22 R_L
%	V/m		m	m
0	60	–	(80)	(260)
100	0,01	–	495 000	1 550 000
10^{-1}	0,32	0,33	15 652	49 193
10^{-2}	1,00	1,00	4 950	11 556
10^{-3}	3,16	3,16	1 565	4 919
10^{-4}	9,86	10,00	495	1 556

By expressing the RSA boundaries in terms of a field strength, and not, for example, in terms of the distance between the transmitter and the point of observation, Equation (15) is applicable to any transmitter producing a field strength which is inversely proportional to the distance. However, after the classes have been established, a certain transmitter will have a certain value of the constant of proportionality k. Then class boundaries can be associated with distances $R_L = (k/P)/E_L$ between transmitter and point of observation. In Table 8 examples of R_L are given, assuming k = 7 (as in the case of a half-wave dipole) and k = 22 (the worst-case value found in 4.4.2.2), while the transmitter power P = 500 kW. The R_L values for E_L = 60 V/m have been put in between brackets, because, in the considered frequency range, the far-field condition is not valid at these distances.

The advantage of choosing the field-strength boundaries first is that the classes are the same for all kinds of transmitter, while the choice of a class is then determined by the probability that victim equipment will be at a certain distance from the chosen class of transmitters. In general, an estimate of the latter probability is easier than an estimate of the field-strength probability.

4.4.3.3 Asymmetrical-voltage classification

A classification of the induced open-circuit common-mode voltage U_h may be based on the probability $pr\{U_h \geq U_L\}$ that U_h is equal to or larger than a given limit value U_L. If $f_t(G)$ describes the truncated distribution of G factors (see 4.4.2.3.4), $f_n(H_o)$ the normalized field-strength distribution and use is made of the relation $U_h = G_o \times H_o$, in Annex C it is shown that this probability can formally be written as

Documents
Document Sharing Hub
Full document details: PD CISPR TR 16-3:2020